

High-fidelity simulations of gravity currents using a high-order finite-difference spectral vanishing viscosity approach

Ricardo A. S. Frantz^{a,b}, Georgios Deskos^c, Sylvain Laizet^{d,*}, Jorge H. Silvestrini^a

^a*School of Technology, Pontifical Catholic University of Rio Grande do Sul, Porto Alegre, Brazil*

^b*DynFluid, Arts et Métiers, 151 Bd. de l'Hôpital, 75013 Paris, France*

^c*National Wind Technology Center, National Renewable Energy Laboratory, Golden, Colorado 80401, USA*

^d*Department of Aeronautics, Imperial College London, London, SW7 2AZ, UK*

Abstract

This numerical work investigates the potential of a high-order finite-difference spectral vanishing viscosity approach to simulate gravity currents at high Reynolds numbers. The method introduces targeted numerical dissipation at small scales through altering the discretisation of the second derivatives of the viscous terms in the incompressible Navier-Stokes equations to mimic the spectral vanishing viscosity (SVV) operator, originally designed for the regularisation of spectral element method (SEM) solutions of pure advection problems. Using a sixth-order accurate finite-difference scheme, the adoption of the SVV method is straightforward and comes with a negligible additional computational cost. In order to assess the ability of this high-order finite-difference spectral vanishing viscosity approach, we performed large-eddy simulations (LES) of a gravity current in a channelised lock-exchange set-up with our SVV model and with the well-known explicit static and dynamic Smagorinsky sub-grid scale (SGS) models. The obtained data are compared with a direct numerical simulation (DNS) based on more than 800 million mesh nodes, and with experimental measurements. A framework for the energy budget is introduced to investigate the behaviour of the gravity current. First, it is found that the DNS is in good agreement with the experimental data for the evolution of the front location and velocity field as well as for the stirring and mixing inside the gravity current. Secondly, the LES performed with less than 0.4% of the total number of mesh nodes compared to the DNS, can reproduce the main features of the gravity currents, with the SVV model yielding slightly more accurate results. It is also found that the dynamic Smagorinsky model performs better than its static version. For the present study, the static and dynamic Smagorinsky models are 1.8 and 2.5 times more expensive than the SVV model, because the latter does not require the calculation of explicit SGS terms in the Navier-Stokes equations nor spatial filtering operations.

Keywords: large-eddy simulation, direct numerical simulation, high-order finite-difference schemes, spectral vanishing viscosity, gravity current, lock-exchange

*Corresponding author

Email address: s.laizet@imperial.ac.uk (Sylvain Laizet)

1. Introduction

Gravity or density currents are commonly found in many physical processes involving the mixing between two fluids of different densities. They are driven by the density difference between a heavy fluid and a lighter ambient fluid. In nature, they can travel over long distances, up to hundreds of kilometres, in lakes, seas and oceans, with flow speeds of up to 20 m s^{-1} even on nearly flat floors (Piper et al., 1999). The density difference can be caused by temperature, salinity or solid material in suspension. Examples of such flow phenomena are cold fronts, seafloor turbidity currents, snow avalanches, riverine plumes, pyroclastic lava flows, or anthropogenic like oil spills in the oceans and gas leaks in the atmosphere, and debris flows in urban areas from buildings collapse (Simpson, 1999; Allen, 2012). Understanding the physical mechanisms associated with these currents as well as the correct prediction of their main features are of great importance for practical and theoretical purposes. Gravity currents observed in nature are complex, very voluminous and are extremely challenging and costly to study. As a result, they have been mainly investigated in very simplified configurations such as the lock-exchange set-up (often in a channel configuration) where a sliding gate separates two volumes of fluid at rest; one volume contains a heavy fluid and the other a light one. When the gate is removed, differences in hydrostatic pressure generate a dense current moving along the bottom wall, while a neutrally buoyant current travels in the opposite direction along the top wall or free surface. Different phases of spreading have been identified for gravity currents in the lock-exchange set-up: (i) an acceleration phase where the current initially at rest reaches its maximum velocity, (ii) a slumping phase with a nearly constant front velocity, (iii) an inertial phase for which the buoyancy driving force is balanced by inertia and during which the current starts to decelerate, and (iv) a viscous phase for which the buoyancy driving force is balanced by viscosity (Huppert and Simpson, 1980; Bonnetaze et al., 1993; Huppert and Simpson, 1980; Cantero et al., 2007b). Note that the last two phases are sometimes referred to as self-similar phases (Huppert and Simpson, 1980), although in some set-ups (e.g. short tanks or high concentrations) the viscous phase may not be observed. Contrarily, low Reynolds number cases (e.g. low concentration flows), the current may rapidly shift to a viscous dominated phase of spreading without experiencing an inertial phase (see Cantero et al. (2008) for details). Turbulent structures have also been identified as key components of the dynamics of gravity currents. Instabilities originating from the shear between the current and the ambient flow, as well as the near-wall high- and low-speed streaks, lead to well-known “lobe and cleft” structures located at the head of the current (Härtel et al., 2000; Espath et al., 2015). These coherent structures also enhance the exchange of mass and momentum between the ambient (lighter) and current (heavier) fluids, enabling mixing through turbulent entrainment (Ellison and Turner, 1959; Fragozo et al., 2013; Sher and Woods, 2015; van Reeuwijk et al., 2018).

To establish most of the existing knowledge on gravity currents, detailed experimental studies (Britter and Simpson, 1978; Britter and Linden, 1980; Rottman and Simpson, 1983; Gladstone et al., 1998; de Rooij and Dalziel, 2001; Shin et al., 2004; Nogueira et al., 2014; Sher and Woods, 2015, 2017; Ottolenghi et al., 2017; Zemach et al., 2019; Martin et al., 2019, 2020; De Falco et al., 2020, 2021) and direct numerical simulations (DNS) (Necker et al., 2002, 2005; Cantero et al., 2007a; Nasr-Azadani and Meiburg, 2014; Espath et al., 2014; Zgheib et al., 2015; Francisco et al., 2018) have been employed in simplified configurations. DNS requires the flow field to be resolved adequately down to

the smallest turbulent scales, where the energy of the flow is dissipated into heat. With
48 such resolution requirements and current petascale supercomputers, DNS for gravity
currents are limited to moderate Reynolds numbers, typically $Re \sim \mathcal{O}(10^4)$. DNS at
higher Reynolds numbers are in theory possible but require a substantial amount of
51 computational resources. On the other hand, large-eddy simulation (LES) is another
widely used strategy to numerically study turbulent flows thanks to its ability to capture
the main turbulent scales of the flow at a much lower cost than DNS, see [Meneveau and](#)
54 [Katz \(2000\)](#); [Sagaut \(2006\)](#) for an introduction.

LES has emerged recently as an appropriate tool to study the main features of gravity
currents ([Constantinescu, 2014](#); [Meiburg et al., 2015](#)). In LES, the mesh resolution is fine
57 enough to accurately approximate the dynamic of most of the turbulent scales (up to a
filter/mesh scale) while the contribution of the unresolved small scales is modelled. The
traditional presentation of LES is based on the introduction of low-pass filtering to define
60 the large-scale part of the flow whereas the residual part from the filtering operation is re-
ferred to as the subgrid-scale (SGS) part. LES can provide answers to more-realistic, and
higher-Reynolds-number problems, however, it relies on the adequate modelling of the
63 energy transfers between the resolved and the SGS which is often parametrised through
structural eddy viscosity models ([Smagorinsky, 1963](#); [Germano et al., 1991](#); [Meneveau](#)
[and Lund, 1997](#); [Vreman, 2004](#)). Inherently, the selection of the SGS model and the cor-
66 rect tuning of its parameters can dramatically affect the quality of the solution. Moreover,
the interaction of the different LES parametrisations with the underlying numerical er-
rors of the discretisation schemes was shown to be an important factor for accuracy
69 ([Vreman et al., 1996](#); [Ghosal, 1996](#); [Chow and Moin, 2003](#)). To this end, implicit LES
(iLES) methodologies, which utilise purely dissipative numerical schemes (e.g. upwinding
schemes), have become viable alternative solutions in LES studies by combining numerical
72 and physical parametrisations ([Boris et al., 1992](#); [Grinstein and Fureby, 2004](#)).

More recently, a new class of dissipation-inducing numerical schemes have emerged for
high-order methods originating from the concept of spectral vanishing viscosity (SVV)
75 proposed by [Tadmor \(1989\)](#). While the method was originally proposed for regularis-
ing spectral solutions of the Burger's equations, it was later employed to control high-
wavenumber oscillations in the context of the incompressible Navier-Stokes equations
78 ([Karamanos and Karniadakis, 2000](#); [Kirby and Karniadakis, 2002](#); [Pasquetti, 2005](#); [Pas-](#)
[quetti et al., 2008](#)). Unlike the previously mentioned implicit LES schemes (which often
rely on upwind schemes to add numerical dissipation), SVV adds dissipation exclusively
81 to smaller scales, as defined by the mesh cut-off scale. A recent effort to employ the
concept of SVV in higher-order compact finite difference schemes was proposed by [Lam-](#)
[ballais et al. \(2011\)](#), in which a numerical kernel was designed to manipulate numerical
84 errors of the viscous term in the incompressible Navier-Stokes equations (via customised
finite-difference schemes for the second derivatives). The strategy was initially aimed
at controlling dispersive and aliasing errors at near cut-off scales. Due to its excellent
87 performance, it was later extended and successfully applied to LES studies of isotropic
turbulence (i.e. Taylor-Green vortex, [Dairay et al. \(2017\)](#)) as well as more complex flows
(e.g. jets, wakes, etc.) ([Dairay et al., 2014](#); [Ioannou and Laizet, 2018](#); [Deskos et al.,](#)
90 [2019](#)).

For gravity currents, several LES studies have been performed in recent years, mainly
based on an explicit SGS model approach. A review of LES of gravity currents was pre-

93 sented in [Constantinescu \(2014\)](#) along with new results based on a dynamic Smagorinsky
model and a non-dissipative viscous flow solver. This work discussed how the evolution
and structure of gravity currents change when the Reynolds number is increased to values
96 relevant in nature and environmental engineering applications. LES of lock-exchange in
a channel set-up for a flatbed were performed in [Ooi et al. \(2009\)](#). The LES solver in
this study used a non-dissipative numerical scheme and was combined with the dynamic
99 Smagorinsky model to account for the effect of the SGS stresses. The authors investigated
the effect of the Reynolds number on the near-bed flow structure and the friction velocity
distribution at the bottom of the channel, by performing simulations up to $Re \sim 250,000$.
102 The Reynolds number dependence on mixing for lock-exchange gravity current was inves-
tigating in [Özgökmen et al. \(2009\)](#) using DNS and LES. Six different LES models were
tested and it was found that all LES models provide an improvement with respect to
105 DNS, however, it was not possible to identify a clear and consistent superior LES model.

Gravity currents past circular cylinders mounted above a wall were investigated in
[Gonzalez-Juez et al. \(2010\)](#) using 2D and 3D LES with a focus on the force load on the
108 cylinder and the behaviour of the friction velocity at the bottom wall near it. Their
simulations considered Reynolds numbers in the range of 2,000-45,000. LES were also
employed by [Tokyay et al. \(2011\)](#) and [Tokyay et al. \(2014\)](#) to investigate the structure
and evolution of a gravity current in a channelised lock-exchange set-up with a series of
111 identical large-scale obstacles (dunes and square ribs) at the channel bottom. A dynamic
approach similar to the dynamic Smagorinsky model was used for the unresolved scales
114 (see [Pierce \(2001\)](#) for more details). These studies looked into the effect of the roughness
elements shape and height as well as the Reynolds number dependence on the temporal
variation of the front velocity, mixing, and flow structure of the current. In [Ottolenghi
et al. \(2016a,b\)](#) LES based on the dynamic Smagorinsky model were performed to study
117 mixing and entrainment in unsteady gravity currents down a slope with different initial
density difference and aspect ratio for the released volume. Data were compared with
120 laboratory experiments, and the results showed a reasonable agreement. [Ottolenghi et al.
\(2018\)](#) examined the ability of Lattice-Boltzmann Method (LBM) to reproduce the fun-
damental features of lock-exchange gravity current by performing 2D and 3D LES at
123 different Reynolds numbers. A peculiar modification of the basic LBM, equivalent to
the Smagorinsky model, was employed using an effective collision relaxation time and
obtained good agreement with laboratory data for Reynolds numbers up to $Re = 30,000$.
126 LES of gravity currents in an axisymmetric lock-exchange set-up were performed in [In-
ghilesi et al. \(2018\)](#) for Reynolds numbers spanning several orders of magnitude. Their
results reported hydraulic shocks for high Reynolds numbers which is consistent with re-
129 sults reported of [Grundy and Rottmant \(1986\)](#) where a shallow-water equation solver was
used. LES of lock-exchange gravity currents propagating over a mobile reach were pre-
sented in [Kyrousi et al. \(2018\)](#) to study the underlying mechanisms leading to sediment
132 entrainment for different Reynolds numbers and grain sizes. To model the unresolved
scales in these two studies, the authors used the dynamic Smagorinsky with the constant
evaluated using the Lagrangian procedure of [Meneveau et al. \(1996\)](#) (see [Armenio and
Sarkar \(2002\)](#); [Roman et al. \(2010\)](#) for more details). The choice of the Lagrangian model
135 in these studies was motivated by the absence of directions of homogeneity in the develop-
ment of the currents. Density currents with a continuous release with a jet shape of dense
138 fluid from a finite source down a sloping bed were studied recently in [Chawdhary et al.](#)

(2018). The authors studied the influence of the slope angle and stratification using LES based on a dynamic Smagorinsky model. Several approaches based on LES SGS models, detached eddy simulation (DES), delayed-detached eddy simulation (DDES), Launder-Reece-Rodi (LRR), and $k-\epsilon$ models were evaluated by Emami et al. (2020) for gravity currents in the lock-exchange set-up. It was found that only DES and LES were able to capture the Kelvin-Helmholtz instability and the viscous phase of spreading. More recently, Pelmard et al. (2020) used 200 LES based on the Smagorinsky model to provide a statistical analysis of a lock-exchange gravity current propagating over a 2% slope for a Reynolds number of 60,000, matching the experiments of Wilson et al. (2018). It was found that the front velocity compares very well with analytical scaling laws, as well as experimental and numerical results previously reported. Likewise, the Kelvin-Helmholtz instabilities and the lobe and cleft instabilities at the front were correctly predicted. The authors also discussed the mechanisms of production and destruction of turbulence at the front of the current. The same authors investigated the influence of the mesh resolution in a LES context for a lock-exchange turbidity current (Pelmard et al., 2018). The simulations were performed with a standard Smagorinsky model for a range of Reynolds numbers ranging from transitional currents to fully-developed ones. Spanwise two-point correlations were used to inform on the resolution needed to resolve the largest scales of the current and to check the placement of the LES filter size inside the inertial range.

In the present numerical study, the potential of the high-order finite-difference spectral vanishing viscosity approach of Lamballais et al. (2011) is investigated to simulate accurately gravity currents at high Reynolds numbers. The method can introduce a targeted numerical dissipation at small scales through the discretisation of the second derivatives of the viscous term in the incompressible Navier-Stokes equations, mimicking a conventional spectral vanishing viscosity (SVV) approach. Based on sixth-order accurate finite-difference schemes, the method is straightforward to implement with a negligible computational extra cost by comparison to more conventional explicit LES models. The computational set-up and Reynolds number have been chosen so that they match the experimental measurements of Fragoso et al. (2013). In order to properly assess the potential of this SVV model, a large-scale DNS is also performed in order to compare quantities which are not available experimentally. To the best of our knowledge, this is one of the DNS with the highest Reynolds number for gravity currents in a lock-exchange set-up. LES with the well-known static and dynamic Smagorinsky models are also performed for comparison purposes. A novel framework for the energy budget is also introduced, in order to investigate the behaviour of the gravity current. One originality of the present study is that the LES are performed in the context of highly accurate finite-difference numerical methods. Such methods are desirable in a DNS context due to their ability to provide accurate results. However, in the context of LES, the sensitivity of high-order schemes at small scale can be counterproductive if there is a direct source of numerical errors, such as aliasing (Kravchenko and Moin, 1997) at scales close to the mesh size. In particular, an explicit SGS model designed to reproduce the dissipation of the unresolved scales can be a strong source of numerical errors (the extra non-linearity introduced in the LES equations can produce additional aliasing errors).

The paper is organised as follow: the problem definition, the different LES approaches and the flow solver are described in section 2. The comparison between the experiments of Fragoso et al. (2013) and our DNS is presented in section 3 followed by the LES results

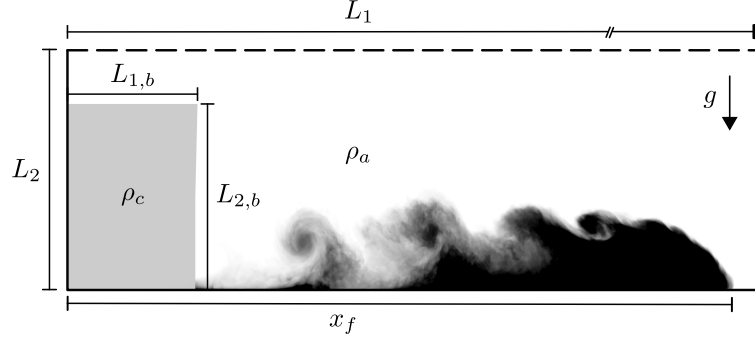


Figure (1) 2D schematic view of a channelised lock-exchange set-up.

186 in section 4. The paper is ended by a summary and conclusion in section 5. A sensitivity study regarding the SVV approach is presented in Appendix A.

2. Problem definition and modelling approaches

2.1. Governing equations

To simulate gravity currents in a channelised lock-exchange set-up, we consider a finite volume release of a heavier fluid (density ρ_c) into a horizontal channel filled with lighter and initially calm ambient fluid (density ρ_a). Schematically, the flow configuration is presented in figure 1. The streamwise direction is x_1 , the vertical direction is x_2 and the spanwise direction is x_3 . The heavier fluid is enclosed in a sub-domain of size $L_{1,b} \times L_{2,b} \times L_3$ in the computational domain of size $L_1 \times L_2 \times L_3$. At the initial time $t = 0$, the heavier fluid is released and the flow is driven purely by gravitational effects. To describe the dynamics of the gravity current mathematically, we make use of the unsteady incompressible Navier-Stokes equations coupled with a density transport equation. The coupling is achieved through a Boussinesq approximation of the gravitational term $(\rho_c - \rho_a)/\rho_a g e_i^g$ where g is the gravity acceleration and $e_i^g = (0, -1, 0)$ represents the unity vector acting in the direction of gravity. In the most generic, non-dimensional and unified (to accommodate both DNS and the various LES approaches) form, the governing equations can be written as

$$\frac{\partial u_i}{\partial x_i} = 0, \quad (1a)$$

$$\frac{\partial u_i}{\partial t} = -\frac{1}{2} \left(u_j \frac{\partial u_i}{\partial x_j} + \frac{\partial u_i u_j}{\partial x_j} \right) - \frac{\partial p}{\partial x_i} + \frac{1}{Re} \mathcal{D} + e_i^g Ri \rho, \quad (1b)$$

$$\frac{\partial \rho}{\partial t} = -u_j \frac{\partial \rho}{\partial x_j} + \frac{1}{Re \cdot Sc} \mathcal{Q} \quad (1c)$$

189 where u_i is the velocity vector field, p the pressure field and ρ is the density field.
 No reference to any filter is explicitly written in the equations. In a LES context, the
 192 unknowns u_i , ρ and p should be interpreted as the large-scale component of velocity,
 density and pressure.

The momentum diffusion term \mathcal{D} can be expressed as

$$\begin{aligned}\mathcal{D} &= \frac{\partial^2 u_i}{\partial x_j \partial x_j} \quad \text{for DNS (see section 2.2),} \\ \mathcal{D} &= \frac{\partial}{\partial x_j} \left[(1 + Re \cdot \nu_t) \left(\frac{\partial u_i}{\partial x_j} + \frac{\partial u_j}{\partial x_i} \right) \right] \quad \text{for explicit LES (see section 2.3),} \\ \mathcal{D} &= \frac{\partial^2 u_i}{\partial x_j \partial x_j} + \frac{\partial}{\partial x_j} \left(Q_c \star \frac{\partial u_i}{\partial x_j} \right) \quad \text{for SVV model (see section 2.4).}\end{aligned}$$

ν_t is the eddy viscosity computed by an explicit LES model. Q_c is a hyperviscous kernel used to construct the SVV operator through a convolution operation (\star), as explained in section 2.4. It will be shown that the hyperviscous kernel, although conceptualised purely in the spectral (wavenumber) domain, is meant for and applied only to the physical domain. The non-linear term of the momentum equation is computed in the skew-symmetric form for increased stability and to reduce aliasing errors (Kravchenko and Moin, 1997), while the non-linear transport term is evaluated in its non-conservative form due to the use of different types of boundary conditions for the density field and velocity fields. The density diffusion term \mathcal{Q} is defined in a similar fashion to the momentum diffusion term \mathcal{D} (the operators for the derivatives in \mathcal{Q} are the same as the operators in \mathcal{D}). Nonetheless, irrespective of the viscous/density diffusion operators formulation the non-dimensional governing equations are both expressed in terms of the Reynolds (Re) and Richardson (Ri) numbers. Their magnitude will ultimately change the physical characteristics of turbulence and therefore should be defined and computed with respect to the problems physical parameters. Thus, based on the initial density difference between the heavier and ambient fluid as well as the initial height $L_{2,b}$ of the heavy fluid column we apply an energy balance,

$$\frac{1}{2} \rho_c U_b^2 = \frac{1}{L_{2,b}} \int_0^{L_{2,b}} g(\rho_c - \rho_a) x_2 dx_2, \quad (3)$$

to obtain a characteristic (or buoyancy) velocity scale $U_b = \sqrt{g' L_{2,b}}$, where $g' = g(\rho_c - \rho_a)/\rho_a$. Here we also assume for the energy balance that the entire dynamic energy of the initial set-up is converted to kinetic energy without any losses. This assumption although not valid (due to viscous effects), allows us to define global characteristic scales for the velocity and time variables. With this definition, the characteristic global Reynolds number can be expressed as

$$Re = \frac{U_b L_{2,b}}{\nu}, \quad (4)$$

where ν is the kinematic viscosity assumed to be the same for the two fluids. Similarly, the overall (bulk) Richardson number is given by

$$Ri = \frac{g' L_{2,b}}{U_b^2}. \quad (5)$$

Note that the choice of $L_{2,b}$ as characteristic length scale leads to $Ri = 1$. Additionally, we may define a dimensionless time scale $\tau = L_{2,b}/U_b$ which can be used to scale the time evolution of the gravity current. Finally, for the density transport the Schmidt (or Prandtl in the case of temperature) number $Sc = \nu/\kappa$ is defined based on a (constant)

222 molecular diffusivity coefficient of the stratifying agent κ and is set to unity to avoid the
 use of finer meshes. It has been shown in [Bonometti and Balachandar \(2008\)](#) that the
 Schmidt number only weakly influences the structure and dynamics of gravity currents
 225 if the Reynolds number of the flow is large, $O(10^4)$ or more. On the contrary, gravity
 currents at low to moderate Reynolds numbers are dependant on the Schmidt number as
 the structure of the mixing region and the front velocities can be modified by diffusion
 228 effects.

Regarding boundary conditions and initial conditions, a no-slip boundary condition
 is applied for the velocity for $x_2 = 0$ while free-slip boundary conditions for $x_1 = 0$,
 231 $x_1 = L_1$ and $x_2 = L_2$ and periodic boundaries in the spanwise direction are imposed. For
 the density, a zero-flux ($\partial\rho/\partial x_i = 0$) boundary condition is applied everywhere ($x_1 = 0$,
 $x_1 = L_1$, $x_2 = 0$, $x_2 = L_2$), except in the spanwise direction where periodic boundary
 234 conditions are imposed. For the initial condition, the density concentration is prescribed
 by

$$\rho(x_1, x_2, x_3, t = 0) = 0.5 - 0.5 \tanh[\delta_b(x_1 - L_{1,b})]. \quad (6)$$

In this work, the value $\delta_b = 20$ was found sufficient to avoid discontinuities in the deriva-
 237 tives while having a sharp enough profile to reproduce a virtual gate, even for the coarse
 mesh of the LES. Furthermore, the initial spatially-averaged velocity field is zero every-
 where in the domain with white noise (corresponding to an initial kinetic energy of 1%)
 240 superposed to all velocity components at the gate position ($x = L_{1,b}$) in order to trigger
 flow instabilities (similar to the removal of the gate in an experiment).

2.2. Flow solver

243 The simulations in this study are carried out within the open-source, turbulence
 simulation framework **Xcompact3D**¹, designed for DNS and LES of incompressible and
 low-Mach number flows using a Cartesian mesh and high-order finite-difference schemes
 246 ([Laizet and Lamballais, 2009](#); [Laizet and Li, 2011](#); [Bartholomew et al., 2020](#)). The in-
 compressible flow solver within **Xcompact3D** is called **Incompact3d** and is based on sixth-
 order compact finite-difference schemes ([Laizet and Lamballais, 2009](#)) for the spatial-
 249 discretisation and a fractional-step method using a third-order explicit Adams-Bashforth
 method for the temporal integration (other time schemes are available, depending on the
 flow configuration). Within the fractional-step method, the incompressibility condition is
 252 dealt with by directly solving a Poisson equation in spectral space using 3D Fast Fourier
 Transforms and the concept of the modified wavenumber ([Lele, 1992](#)). The velocity-
 pressure mesh arrangement is half-staggered to avoid spurious pressure perturbations
 255 ([Laizet and Lamballais, 2009](#)).

The simplicity of the mesh allows an easy implementation of a 2D domain decompo-
 sition based on pencils ([Laizet and Li, 2011](#)). The computational domain is split into
 258 a number of sub-domains (pencils) which are each assigned to an MPI-process. The
 derivatives and interpolations in the x-direction (y-direction, z-direction) are performed
 in X-pencils (Y-pencils, Z-pencils), respectively. The 3D FFTs required by the Pois-
 261 son solver are also broken down as a series of 1D FFTs computed in one direction at
 a time. Global transpositions to switch from one pencil to another are performed with

¹Freely available at github.com/xcompact3d/

the MPI command `MPI_ALLTOALL(V)`. The flow solvers within `Xcompact3D` can scale well
 264 with up to hundreds of thousands of MPI-processes for simulations with several billion
 mesh nodes (Laizet and Li, 2011). The `Xcompact3D` framework has been used recently
 to perform DNS of Boussinesq gravity currents in various set-up and for a wide range of
 267 Reynolds numbers (Espath et al., 2014, 2015; Francisco et al., 2018; Lucchese et al., 2019)
 and DNS of non-Boussinesq gravity currents (Bartholomew and Laizet, 2019). Finally,
 further validation and verification studies of the code for the SVV model and the explicit
 270 LES models can be found in: Dairay et al. (2014, 2017); Ioannou and Laizet (2018);
 Deskos et al. (2019); Schuch et al. (2018); Deskos et al. (2020).

2.3. Explicit SGS modelling

In this study, two reference explicit SGS models have been tested for comparison with
 the present SVV approach. Explicit LES relies on the direct modelling of the velocity
 and density subgrid-scale (SGS) stresses which appear in the momentum and density
 transport equations. To this end, the eddy viscosity ν_t and diffusivity κ_t variables are
 defined to approximate the subgrid-scale (SGS) stresses under the Boussinesq hypothesis,

$$\tau_{ij} = -2\nu_t S_{ij} \quad (7a)$$

$$q_j = -\kappa_t \frac{\partial \rho}{\partial x_j} \quad (7b)$$

273 where $S_{ij} = 0.5(\frac{\partial u_i}{\partial x_j} + \frac{\partial u_j}{\partial x_i})$ is the strain rate tensor. The eddy viscosity ν_t and eddy
 diffusivity κ_t are connected through the turbulent Schmidt number, $\kappa_t = \nu_t/S_{c_t}$. In
 our simulations the turbulent Schmidt number is set to unity as in the vast majority of
 276 numerical studies of gravity currents. Alternatively, an empirical relationship to scale
 S_{c_t} as function of the coupling term can be sought (see Venayagamoorthy et al. (2003);
 Mahdunia et al. (2011)). The eddy viscosity can be modelled using a functional approach
 279 such as the ones afforded by the standard or dynamic Smagorinsky models (Smagorinsky,
 1963; Germano et al., 1991). Starting with the standard Smagorinsky model (SSM), the
 eddy viscosity is assumed to be proportional to the magnitude of the strain rate $|S|$ as well
 282 as a length scale $l_S = C_S \Delta$ which is proportional to the mesh scale $\Delta = \sqrt[3]{\Delta x_1 \Delta x_2 \Delta x_3}$
 and an empirical coefficient C_S ,

$$\nu_t = C_S^2 \Delta^2 |S|. \quad (8)$$

The empirical coefficient $C_S = 0.15$ is chosen for the simulations which is close to the
 285 theoretical value proposed by Lilly (1966) for isotropic and homogeneous turbulence (a
 preliminary study confirmed that this value was the optimal value for the present set-
 up). The SSM has enjoyed popularity over the years thanks to its simple implementa-
 288 tion, however, it has been found to behave over-dissipatively near walls and/or within
 turbulence-transition regions (Meneveau and Katz, 2000). To this end, an alternative
 calculation of the eddy viscosity was proposed by Germano et al. (1991) to adjust the
 291 Smagorinsky coefficient C_S in both space and time through a purely dynamic procedure.
 The model is based on Germano's algebraic identity (Germano et al., 1991) which relates
 subgrid/filter-scale stresses computed at two different levels,

$$\mathcal{L}_{ij} = T_{ij} - \widetilde{\tau}_{ij} = \widetilde{u_i u_j} - \widetilde{u}_i \widetilde{u}_j \quad (9)$$

294 where $T_{ij} = \widetilde{u_i u_j} - \widetilde{u_i} \widetilde{u_j}$ are the test filter level scale stresses, and $\widetilde{\tau_{ij}}$ are the subgrid-
 scale stresses filtered at the test filter scale. Note that $\widetilde{(\dots)}$ denotes the test filter level
 297 Smagorinsky just described in the previous paragraph and using Lilly's least-squares nor-
 malisation technique [Lilly \(1992\)](#) we may obtain an expression for the DS eddy viscosity,

$$\nu_t = \frac{1}{2} \left\langle \frac{\mathcal{M}_{ij} \mathcal{L}_{ij}}{\mathcal{M}_{kl} \mathcal{M}_{kl}} \right\rangle_{x_3} \Delta^2 |S|, \quad (10)$$

where

$$\mathcal{M}_{ij} = 2\Delta^2 |\widetilde{S}| \widetilde{S}_{ij} - 2\widetilde{\Delta}^2 |\widetilde{S}| \widetilde{S}_{ij}. \quad (11)$$

300 $\langle \rangle_{x_3}$ corresponds to an average in the spanwise direction (homogeneous direction of the
 current). The eddy viscosity and diffusivity are subsequently used in the momentum and
 density diffusion terms for their calculations as discussed in sub-section 2.1.

303 2.4. Spectral Vanishing Viscosity

Spectral vanishing viscosity (SVV) used as a LES model has its roots in the concepts
 of spectral and hyper eddy viscosity ([Kraichnan, 1976](#); [Cerutti et al., 2000](#); [Haugen and
 306 Brandenburg, 2004](#)). The key idea of spectral eddy viscosity as discussed by [Kraichnan
 \(1976\)](#) is that if one closely examines how eddy viscosity acts upon different wavenum-
 ber modes, then it can be shown that eddy viscosity must be allowed to depend upon
 309 the wavenumber magnitude. With this development, wavenumber dependent or simply
 spectral eddy viscosity (SEV) models were devised and applied in the spectral domain
 by [Chollet and Lesieur \(1981\)](#); [Lesieur and Rogallo \(1989\)](#); [Métais and Lesieur \(1992\)](#).
 312 For more information on SEV models, the reader is referred to the review of [Lesieur and
 Métais \(1996\)](#). On the other hand, [Haugen and Brandenburg \(2004\)](#) undertook high-
 Reynolds number turbulence simulation by using the concept of hyperviscosity ($\nu \nabla^6 \mathbf{u}$
 315 instead of $\nu \nabla^2 \mathbf{u}$) and observed no significant differences as far as the inertial region or
 the bottleneck phenomenon ([Falkovich, 1994](#)) of the energy spectra is concerned, while
 significantly reducing their mesh resolution. Spectral vanishing viscosity combines the
 318 two models by conceptualising eddy viscosity in the spectral domain but applying it in
 the physical domain in a form similar to hyperviscosity. The SVV operator is imple-
 mented by multiplying the Fourier coefficients of the velocity field, u_i , with the Fourier
 321 coefficients of a smooth SVV kernel Q_c ,

$$\nu_0 \frac{\partial}{\partial x_j} \left[Q_c \star \frac{\partial u_i}{\partial x_j} \right] = -\nu_0 \sum_{k_0 \leq |k| \leq k_c} k^2 \widehat{Q}_c \widehat{u}_k e^{ikx_k} \quad (12)$$

where ν_0 is the magnitude of SVV, \star denotes a convolution operator and k_n and k_0 are the
 cut-off wavenumber (defined by the mesh size) and the wavenumber above which SVV is
 324 activated, respectively. The Fourier coefficients of the smooth kernel, may be expressed
 via an exponential function following [Karamanos and Karniadakis \(2000\)](#)

$$\widehat{Q}_c(k) = \exp \left[- \left(\frac{k - k_c}{\gamma k_c - k} \right)^2 \right], \quad \text{for } k \geq \gamma k_c. \quad (13)$$

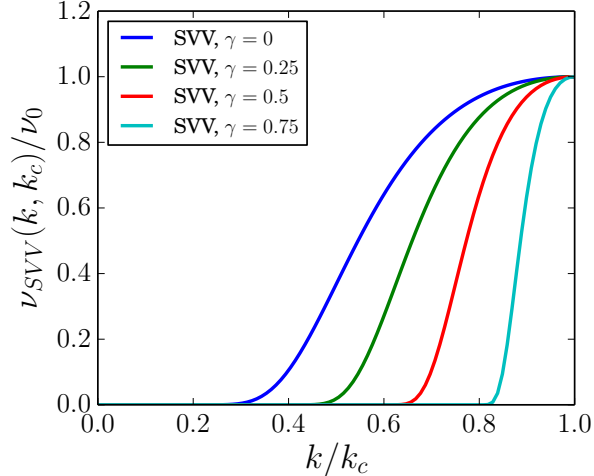


Figure (2) Normalised SVV kernels as a function of the normalised wavenumber k/k_c for different γ .

This kernel is different from the original Heaviside function proposed by [Tadmor \(1989\)](#) and it can be argued that it exhibits a number of advantages. It should be noted that one may easily change the shape of the kernel by changing the value of γ . With increasing γ the SVV kernel becomes steeper and thus affects only the smaller length-scales. On the other hand, as γ becomes smaller, the range of the scales affected by eddy viscosity is broadened, which better resembles the behaviour of a spectral eddy viscosity model. For our study, a value $\gamma = 0.3$ is chosen as it is the value which gives the closest match with the exponential model of [Karamanos and Karniadakis \(2000\)](#). The effect of parameter γ is shown in figure 2 where the wavenumber range in which the SVV viscosity is applied (and its respective amplitude) appears to decrease with increasing γ . The implementation of the discrete SVV kernel in the framework of high-order compact finite-differences is discussed in sub-section 2.5. Compared to the hyperviscosity model, e.g. [Haugen and Brandenburg \(2004\)](#), spectral vanishing viscosity differs in that the amount of dissipation added to the solution is active only after a particular wavenumber and therefore does not affect large energetic scales (triad interaction between the resolved scales). Finally, regarding determining the magnitude of eddy viscosity ν_0 , most previous studies have relied on a “trial-and-error” approach, and an optimum value is often selected based on a better agreement with the reference data. In recent work, however, [Dairay et al. \(2017\)](#) determined the magnitude of SVV in the context of isotropic turbulence using Pao’s equilibrium energy spectrum. This approach will be considered here together with several other values for ν_0 . An alternative approach is that of using the dynamic SVV model ([Kirby and Karniadakis, 2002](#); [Deskos et al., 2019](#)) in which the spectral eddy viscosity is scaled locally by the magnitude of the strain-rate tensor. Such an approach for gravity currents was tested in a preliminary study and did not provide an improvement in the quality of the solution when compared to the approach used in the present work.

2.5. Implementation of the SVV and filtering operators using high-order finite-difference schemes

The high-order strategy considered in this study for accuracy is based on finite-difference schemes implemented on a Cartesian mesh. The main advantages of this specific numerical configuration being its simplicity and efficiency ([Lele, 1992](#); [Laizet](#)

and Lamballais, 2009). The second order derivatives in the momentum diffusion term \mathcal{D} and density diffusion term \mathcal{Q} are based on a compact (implicit) finite-difference scheme, with a 3-9 node stencil:

$$\alpha f''_{i-1} + f''_i + \alpha f''_{i+1} = a \frac{f_{i+1} - 2f_i + f_{i-1}}{\Delta x^2} + b \frac{f_{i+2} - 2f_i + f_{i-2}}{4\Delta x^2} + c \frac{f_{i+3} - 2f_i + f_{i-3}}{9\Delta x^2} + d \frac{f_{i+4} - 2f_i + f_{i-4}}{16\Delta x^2}, \quad (14)$$

where $f_i = f(x_i)$ and $f''_i = f''(x_i)$ represent discrete approximations of the function $f(x)$ and its second derivative $f''(x)$ at nodes $x_i = (i-1)\Delta x$ where Δx is the uniform mesh spacing. Such schemes have a so-called quasi-spectral behaviour (Lele, 1992) due to their capabilities to represent accurately a wide range of scales. A Fourier analysis for such schemes, for which $f(x)$ and $f''(x)$ are decomposed and analysed in the Fourier space ($\hat{f}''_l = -k^2 \hat{f}_l$, where \hat{f}_l and \hat{f}''_l are Fourier coefficients and k^2 are the associated wavenumbers), can provide an effective way to quantify their resolution characteristics (Lele, 1992). A Fourier analysis of the above scheme yields a modified wavenumber,

$$k''(k) = \frac{2a[1 - \cos(k\Delta x)] + \frac{b}{2}[1 - \cos(2k\Delta x)] + \frac{2c}{9}[1 - \cos(3k\Delta x)] + \frac{d}{8}[1 - \cos(4k\Delta x)]}{\Delta x^2[1 + 2\alpha \cos(k\Delta x)]}. \quad (15)$$

which depends on coefficients (α, a, b, c, d). These coefficients are determined based on a desired formal accuracy of the second derivative (e.g fourth- or sixth-order accuracy) by satisfying the following equations in an accumulating order,

$$a + b + c + d = 1 + 2\alpha \quad (\text{second order}) \quad (16a)$$

$$a + 2^2b + 3^2c + 4^2d = \frac{4!}{2!}\alpha \quad (\text{fourth order}) \quad (16b)$$

$$a + 2^4b + 3^4c + 4^4d = \frac{6!}{4!}\alpha \quad (\text{sixth order}) \quad (16c)$$

$$a + 2^6b + 3^6c + 4^6d = \frac{8!}{6!}\alpha \quad (\text{eight order}) \quad (16d)$$

$$a + 2^8b + 3^8c + 4^8d = \frac{10!}{8!}\alpha \quad (\text{tenth order}). \quad (16e)$$

For example, by satisfying all equations up to (16c) the coefficients are calculated to be equal to $\alpha = 2/11$, $a = 12/11$, $b = 3/11$ and $c = d = 0$ and the approximation is sixth-order accurate (Lele, 1992). The rationale here is to obtain the desired accuracy with the smallest possible stencil while keeping the implicit character of the scheme, hence the choice of $c = d = 0$. Following however Lamballais et al. (2011) a discrete SVV operator may be constructed by allowing k'' to mimic the behaviour of the analytical model of Karamanos and Karniadakis (2000) for which the extra numerical viscosity can be expressed as

$$\frac{\nu_{SVV}(k, k_c)}{\nu_0} = \begin{cases} 0 & \text{if } k < 0.3k_c \\ \exp \left[- \left(\frac{k_c - k}{0.3k_c - k} \right)^2 \right] & \text{if } 0.3k_c \leq k \leq k_c, \end{cases} \quad (17)$$

where $k_c = \pi/\Delta x$ is the mesh cut-off wavenumber. It is possible to customise the finite-difference scheme 14 to mimic this SVV operator while maintaining a sixth-order accuracy by satisfying all equations up to (16c). However two more constraints need to be added to the system of equations at $k = k_m = 2/3k_c$ and $k = k_c$ so that

$$k''(k_c) = \left(1 + \frac{\nu_0}{\nu}\right)k_c^2, \quad (18a)$$

$$k''(k_m) = \left(1 + 0.437\frac{\nu_0}{\nu}\right)k_m^2. \quad (18b)$$

where ν_0/ν is set to be the desired ratio between the SVV magnitude ν_0 and the background kinematic viscosity ν . Equations (18a) and (18b) are determined by requiring $-\nu k''(k) = -[\nu + \nu_{SVV}(k)]k^2$ at both $k = k_c$ and $k = k_m = 2/3k_c$. With these two constraints and to keep a sixth-order accuracy, the set of coefficients for the scheme 14 can be expressed as,

$$\alpha = \frac{1}{2} - \frac{320k_m''\Delta x^2 - 1296}{405k_c''\Delta x^2 - 640k_m''\Delta x^2 + 144} \quad (19a)$$

$$a = -\frac{4329k_c''\Delta x^2/8 - 32k_m''\Delta x^2 - 140k_c''\Delta x^2 + 286}{405k_c''\Delta x^2 - 640k_m''\Delta x^2 + 144} \quad (19b)$$

$$b = \frac{2115k_c''\Delta x^2 - 1792k_m''\Delta x^2 - 280k_c''\Delta x^2 + 1328}{405k_c''\Delta x^2 - 640k_m''\Delta x^2 + 144} \quad (19c)$$

$$c = -\frac{7695k_c''\Delta x^2/8 + 288k_m''\Delta x^2 - 180k_c''\Delta x^2 - 2574}{405k_c''\Delta x^2 - 640k_m''\Delta x^2 + 144} \quad (19d)$$

$$d = \frac{198k_c''\Delta x^2 + 128k_m''\Delta x^2 - 40k_c''\Delta x^2 - 736}{405k_c''\Delta x^2 - 640k_m''\Delta x^2 + 144}, \quad (19e)$$

375 where k_c'' is the expected value of k'' at the mesh cut-off wavenumber and k_m'' is the expected value of k'' at $2/3$ of the mesh cut-off wavenumber.

378 The resulting discrete “hyper-viscous” operator contains both the SVV and viscous parts. Thus, the actual behaviour of the discrete SVV operator in the wavenumber space can be found only after we separate the viscous part ($-\nu k^2$), from the hyper-viscous part $-\nu k''$, and obtain the actual discrete spectral vanishing viscosity $\nu''(k)$ via

$$-\nu''(k)k^2 = -\nu(k'' - k^2). \quad (20)$$

381 A plot of the final discrete SVV operator is shown in figure 3 together with the analytical function of Karamanos and Karniadakis (2000). The theoretical “modified” wavenumber kernel is equal to $k'' = (1 + \nu''(k)/\nu)k^2$. The discrete SVV kernel is found to be a satisfactory approximation of the analytical operator of Karamanos and Karniadakis (2000) for the whole wavenumber range with only small deviations at the near cut-off $0.75k_c < k < k_c$ and half cut-off $0.4k_c < k < 0.6k_c$ wavenumbers where only small differences in the relative magnitude are observed ($\sim 10 - 20\%$). These differences are not expected to alter either the quality of our results or our conclusions.

387 Regarding the filtering operator required by the dynamic Smagorinsky model, a discrete test filter is constructed using compact finite differences. The filtered fluid property

390

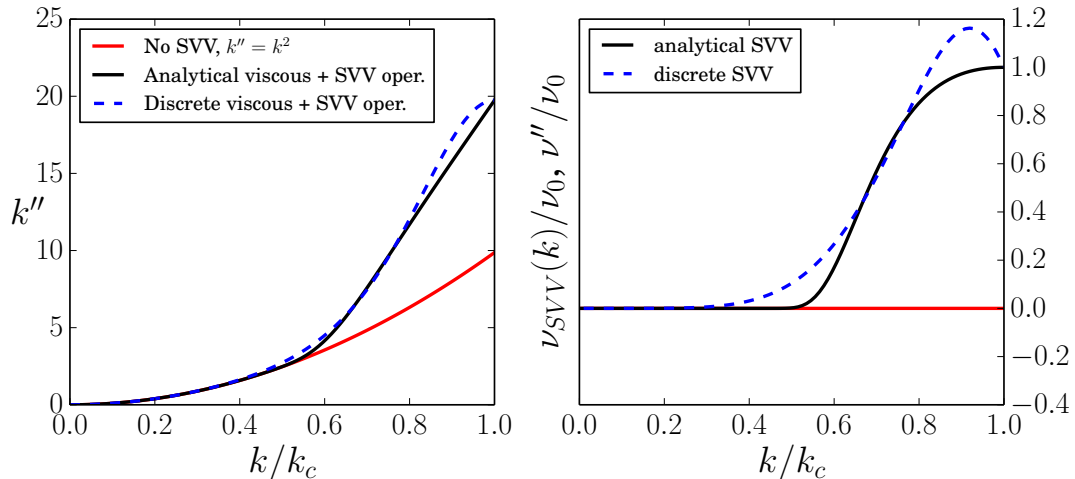


Figure (3) Modified wavenumber k'' and the spectral vanishing viscosity (SVV) kernel for the analytical operator of [Karamanos and Karniadakis \(2000\)](#) and the proposed operator normalised by the SVV magnitude ν_0 .

\hat{f}_i is computed with a 3 – 9 node stencil,

$$\alpha \hat{f}_{i-1} + \hat{f}_i + \alpha \hat{f}_{i+1} = a f_i + \frac{b}{2}(f_{i+1} + f_{i-1}) + \frac{c}{2}(f_{i+2} + f_{i-2}) + \frac{d}{2}(f_{i+3} + f_{i-3}), \quad (21)$$

where the coefficients α, a, b, c, d are set to satisfy sixth-order accuracy which is consistent with the truncation error of all other spatial discrete operators. Hence, the discrete filter coefficients are found to be equal to $a = 0.0625(11 + 10\alpha)$, $b = 0.0312532(15 + 34\alpha)$, $c = -0.0625(3 - 6\alpha)$, $d = 0.03125(1 - 2\alpha)$, where $\alpha \in [-0.5, 0.5]$ is a free user-defined parameter. In our study we have chosen to use $\alpha = 0$ to approximate a Gaussian filter in the wavenumber space, aiming at an effective filter size equal to $\tilde{\Delta} \approx 2\Delta$. Finally, it is noteworthy that for non-periodic boundaries and for stability reasons, filtering at the first mesh node is avoided.

2.6. Energy budget framework

A complete energy budget for gravity currents in the lock-exchange set-up can be extracted from the governing equations and density transport equation, see [Necker et al. \(2005\)](#) and [Espath et al. \(2014\)](#). The energy budget can be used to better understand gravity currents by investigating the temporal evolution of the potential energy, kinetic energy and associated energy transfer mechanisms. In the present study, the conceptual framework of [Winters et al. \(1995\)](#), based on available and background potential energy ([Lorenz, 1955](#)), is adapted to lock-exchange gravity currents. Such a framework, which has been widely used for stratified flows ([Patterson et al., 2006](#); [Oezgoekmen et al., 2009](#); [Fragoso et al., 2013](#); [Ottolenghi et al., 2016a](#); [la Forgia et al., 2018](#)), can distinguish the stirring (a large-scale reversible process) and mixing (a small-scale irreversible process) features of a gravity current. As explained in the experimental reference study of [Fragoso et al. \(2013\)](#), this approach can explicitly capture the changes in potential energy due to adiabatic processes, which transport fluid elements without molecular mass or heat

414 transfer (stirring), from changes due to diabatic processes (mixing). The energy budget
 will be used for comparison with the experimental work of [Fragoso et al. \(2013\)](#) and to
 assess the performance of the LES models.

417 Overall, the total energy \mathcal{T} for the gravity current is equal to

$$\mathcal{T}(t) = \mathcal{P}_a(t) + \mathcal{P}_b(t) + \mathcal{K}(t) + \mathcal{I}(t), \quad (22)$$

where \mathcal{P}_a is the available energy, \mathcal{P}_b is the background energy, \mathcal{K} is the total kinetic energy and \mathcal{I} is the internal energy. The total potential energy \mathcal{P} is defined as

$$\mathcal{P}(t) = \int_V [\rho(x_1, x_2, x_3, t)x_2]dV, \quad (23)$$

420 where the integral is taken over the full computational domain. The background potential energy \mathcal{P}_b is defined as the minimum potential energy attainable through an adiabatic redistribution of the density field. It can be expressed as a function of time as

$$\mathcal{P}_b(t) = \int_V \rho^*(x_1, x_2, x_3, t)x_2dV. \quad (24)$$

423 $\rho^*(x_1, x_2, x_3, t)$ is the density field redistributed in the minimal energy state (see as an example figure 2 of [Fragoso et al. \(2013\)](#)). In our simulations, \mathcal{P}_b is approximated from the 3D density snapshots with the pdf method, sampled with a computationally inexpensive empirical cumulative distribution function (e.c.d.f.), following an approach introduced by [Tseng and Ferziger \(2001\)](#); [Oezgoekmen et al. \(2009\)](#). The available potential energy \mathcal{P}_a is defined as the difference between the total potential energy \mathcal{P} and the background potential energy \mathcal{P}_b

$$\mathcal{P}_a(t) = \mathcal{P}(t) - \mathcal{P}_b(t), \quad (25)$$

Two routes are available for the conversion of available potential energy \mathcal{P}_a to background potential energy \mathcal{P}_b . The first route is associated with stirring. The total kinetic energy \mathcal{K} , defined as

$$\mathcal{K}(t) = \frac{1}{2} \int_V [u_1^2(x_1, x_2, x_3, t) + u_2^2(x_1, x_2, x_3, t) + u_3^2(x_1, x_2, x_3, t)] dV. \quad (26)$$

can be modified via reversible vertical buoyancy flux, defined as

$$\varpi(t) = \int_V \rho(x_1, x_2, x_3, t)u_2(x_1, x_2, x_3, t)dV. \quad (27)$$

435 Changes in total kinetic energy \mathcal{K} can indeed be associated with changes in dissipation (the total kinetic energy will eventually be transformed in heat via dissipation), which will affect the internal energy and ultimately the background energy via density diffusion. The total viscous dissipation can be explicitly computed as

$$\epsilon(t) = \frac{1}{Re} \int_V \frac{\partial u_i(x_1, x_2, x_3, t)}{\partial x_j} \frac{\partial u_i(x_1, x_2, x_3, t)}{\partial x_j} dV, \quad i, j = 1, 2, 3. \quad (28)$$

438 while density diffusion can be defined as

$$\Phi(t) = \frac{1}{ReSc} \int_V x_2 \frac{\partial^2 \rho(x_1, x_2, x_3, t)}{\partial x_i^2} dV \quad i = 1, 2, 3. \quad (29)$$

Viscous dissipation and density diffusion are unidirectional energy mechanisms which act as source and sink of the internal energy, respectively. The internal energy \mathcal{I} can be evaluated as

$$\mathcal{I}(t) = \int_0^t [\epsilon(t) - \Phi(t)] dt. \quad (30)$$

The second route for the conversion of available potential energy \mathcal{P}_a to background potential energy \mathcal{P}_b is a direct route, known as irreversible dyapical mixing. The term dyapical refers to the fact that mixing is a diffusive process across interfaces of different densities (also known as diapycnal surfaces), hence this route is only available in stratified flows as explained in [Winters et al. \(1995\)](#). In the current framework, irreversible dyapical mixing is defined as an irreversible energy transfer mechanism acting towards smoothing gradients of ρ (directly increasing the background potential energy \mathcal{P}_b). Following the work of [Winters et al. \(1995\)](#), irreversible dyapical mixing can be simply defined as the time derivative of

$$\varrho(t) = \dot{\mathcal{P}}_b(t). \quad (31)$$

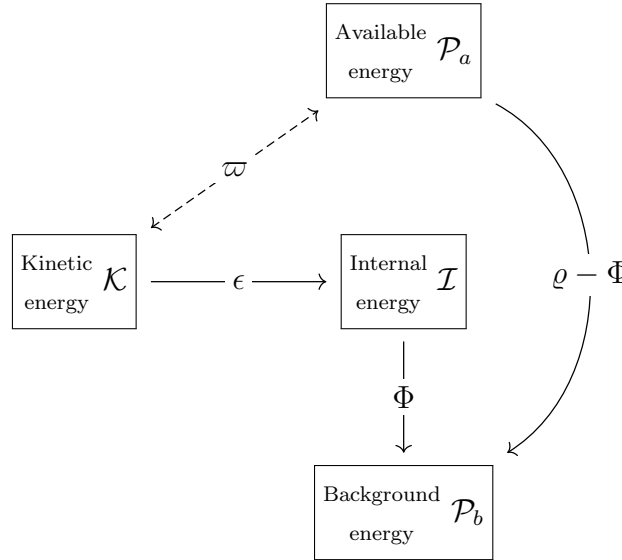


Figure (4) New energy budget framework for gravity currents in a lock-exchange set-up.

The energy budget framework is presented in figure 4, with the distribution of energy among the different terms. Note finally that in the next sections, the energy budget is normalised by the total potential energy at the start of the simulation $\mathcal{P}(t = 0) = \mathcal{T}(t = 0)$.

3. DNS validation against experimental data

The laboratory experiment number 6 of [Fragoso et al. \(2013\)](#) (EX6) has been selected as a reference for comparison with the simulations. It consists of a dense solution (with $g' = 12 \text{ cm s}^{-2}$) made from sugar and water which is placed behind a plastic lock in a $2.4 \text{ m} \times 0.5 \text{ m} \times 0.1 \text{ m}$ tank filled with tap water. The domain size for the simulations is equal to $L_1 \times L_2 \times L_3 = 12 \times 1 \times 0.5$ whereas the initial reservoir $L_{1,b} \times L_{2,b} \times L_3 = 1 \times 1 \times 0.5$. The Reynolds number is equal to 31,000. It should be noted that in the present set-up

462 and reference experiment $L_2 = L_{2,b}$. Only limited experimental data are available for
comparison with the present simulations: (i) instantaneous spanwise-averaged density
465 fields at regular time intervals, (ii) the temporal evolution of the front position and
associated front velocity (extracted from the movies provided with the article); (iii) the
evolution of the dilution based on normalised subareas of specific density thresholds; and
468 (iv) the evolution of available and background potential energy. Hence, the strategy
here is to first perform a DNS, compare the results with the available experimental
data and then assess the performance of the LES models with the DNS data. Note
that the Reynolds number in EX6 is large enough for a LES approach and it remains
471 computationally reachable for a DNS.

For a DNS, all turbulent scales are supposed to be adequately resolved down to
the mesh level. Such requirement, however, imposes certain restrictions on the spatial
474 resolution. According to Pope (2000) the mesh spacing for a DNS (in physical space)
should be $\Delta x \approx 2.1\eta_K$ where $\eta_K = (\nu^3/\varepsilon_K)^{1/4}$ is the Kolmogorov scale, representative of
the smallest scale in a turbulent flow, where viscosity dominates and the turbulent kinetic
477 energy is dissipated into heat. In the definition of η_K , ε_K is considered as the averaged
rate of dissipation of turbulence kinetic energy per unit mass. Note that the computation
of ε_K is not straightforward in the context of gravity currents: the flow is transitional,
480 evolving from a laminar to a highly-turbulent state; there is a significant anisotropy
due to stratification; the flow is inhomogeneous due to the presence of walls and there
are no homogeneous spatial directions for averaging (except the spanwise direction for
483 channelised currents). Finally, the recommendation from Pope (2000) did not take into
account the accuracy of the numerical methods. It is now well-established that, in terms
of accuracy and computational efficiency, the most spectacular gain is obtained using
486 spectral methods based on Fourier or Chebyshev representation (Canuto et al., 2012).
In particular, highly accurate finite-difference numerical methods, with quasi-spectral
properties, are desirable in a DNS context due to their ability to provide flexibility for
489 the boundary conditions (as opposed to purely spectral methods) and accurate results
with a moderate number of mesh nodes when compared to more conventional low-order
schemes.

492 In almost all published DNS studies of gravity currents, no estimate of the Kolmogorov
scale is provided, with usually very little information on mesh requirement for a given
Reynolds number other than a mesh convergence study. Härtel et al. (1997) suggested
495 that the number of mesh nodes required to achieve adequate resolution depends on the
steepness of the initial profile for the concentration field at the gate (in a channelised lock-
exchange set-up, see δ_b in equation 6). The authors also recommended using the same
498 resolution in the streamwise and vertical directions in the middle of the channel while
a much more refined mesh is needed close to the bottom wall to allow for an adequate
resolution of the developing boundary layer. Zgheib et al. (2015) justified their spatial
501 resolution by observing between 4 and 6 decades of decay in the streamwise-spectra of
particle-volume fraction at various times. They also claimed to have similar decay for
other quantities and vertical-spectra and spanwise-spectra. Similar arguments were used
504 in Cantero et al. (2007b) to justify the spatial resolution for DNS of axisymmetric gravity
currents. In Espath et al. (2014, 2015), the authors looked at the energy budget and in
particular at the total energy, which is supposed to be conserved if all the turbulent scales
507 are modelled properly. If the smallest scales of the flow (the dissipative ones) are not

resolved, then an accumulation of energy would appear at the mesh resolution level, and the total energy would not be conserved. Note that this accumulation of energy would also be visible on energy spectra.

The DNS is discretised with $n_1 \times n_2 \times n_3 = 4097 \times 769 \times 257$ mesh nodes and a time step of $\Delta t = 2 \times 10^{-4}$. Note that the mesh is not refined closed to the bottom wall in the vertical direction. This spatial resolution has been chosen after a mesh refinement study to make sure that the solution is independent of the mesh resolution. Expressed in wall viscous units, it corresponds to a maximal resolution of $\Delta x_{1max}^+ \approx 1$, $\Delta x_{2max}^+ \approx 0.5$ and $\Delta x_{3max}^+ \approx 1$. Those values have been obtained by calculating the maximum value of the spanwise-averaged wall shear velocity at each time step. The DNS is performed with 8,192 computational cores on the UK Supercomputing facility [ARCHER](#). The spatial resolution required to capture the smallest scales of the flow adequately was checked by looking at the temporal evolution of the ratio between the spatial resolution and the largest Kolmogorov scale for each time step, see figure 5. The average rate of dissipation of turbulence kinetic energy per unit mass ε_K is evaluated at each time step using the following expression

$$\varepsilon_K = \frac{1}{Re} \frac{\partial u'_i}{\partial x_j} \frac{\partial u'_i}{\partial x_j}, \quad i, j = 1, 2, 3 \quad (32)$$

where the fluctuating velocities u'_i have been obtained by removing the spanwise-averaged mean velocity at each time step. It can be seen in figure 5 that in the vertical direction, the condition $\Delta x_2/\eta_K \leq 2$ is always satisfied while $\Delta x_3/\eta_K \leq 3$ and $\Delta x_1/\eta_K \leq 5$ are satisfied in the spanwise and streamwise directions, respectively. It should be noted that for more than 90% of the simulation, $\Delta x_i/\eta_K \leq 2$, and the largest η_K are located in the head of the gravity current, at the early stages of the simulations, close to the peak of total kinetic energy, see figure 15. It is also important to reiterate that the well-know recommendation from [Pope \(2000\)](#) ($\Delta x_i/\eta_K \approx 2.1$) about resolution requirements does not take into account the order of the numerical schemes. High-order schemes such as the ones used in the present study are able to capture more small scales at a given resolution than low-order schemes. Figure 5 suggests that the mesh resolution is fine enough to take into account the smallest features of the current and a good comparison with the experimental data can be expected. Furthermore, as an extra check for the resolution requirement, figure 15a shows that the total energy in the DNS is perfectly conserved, confirming that the spatial resolution is adequate for the present study.

Figure 6 shows the evolution of the spanwise-averaged density field at $t = 12.4$ and $t = 24$ for the DNS and EX6. Overall, it can be seen that the experimental current and the numerical current are almost identical, with a similar shape, and they seem to be evolving at the same speed. The well-known Kelvin-Helmholtz billows can clearly be seen, especially for the DNS. Few differences can be observed at the interface between the current and its ambient, with a clearer interface for the experiment. This could be attributed to the difficulty in the experiment to capture low thresholds for the density field, as reported in [Fragoso et al. \(2013\)](#). The head of the current is also more pronounced in the simulation (darker red) for $t = 12.4$, suggesting that the current might carry more energy in the DNS than in the experiment. This can be related to the noisy removal of the gate in the experiment which might have consumed extra energy. However, the opposite trend can be observed for $t = 24$, with a more diffuse head for the DNS. It might be related to a more intense mixing activity at the interface for the DNS, which could

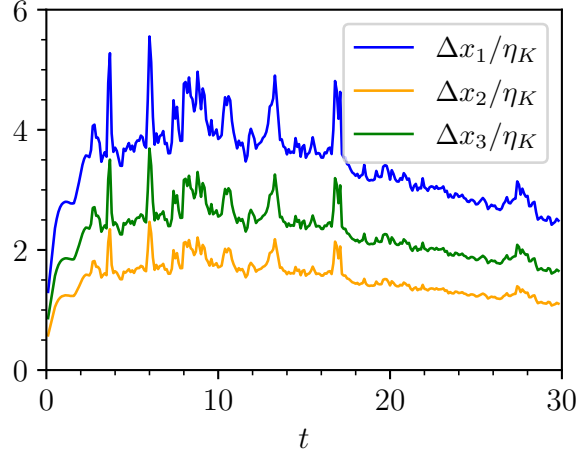


Figure (5) Temporal evolution of the spatial resolution with respect to the Kolmogorov scale for the present DNS.

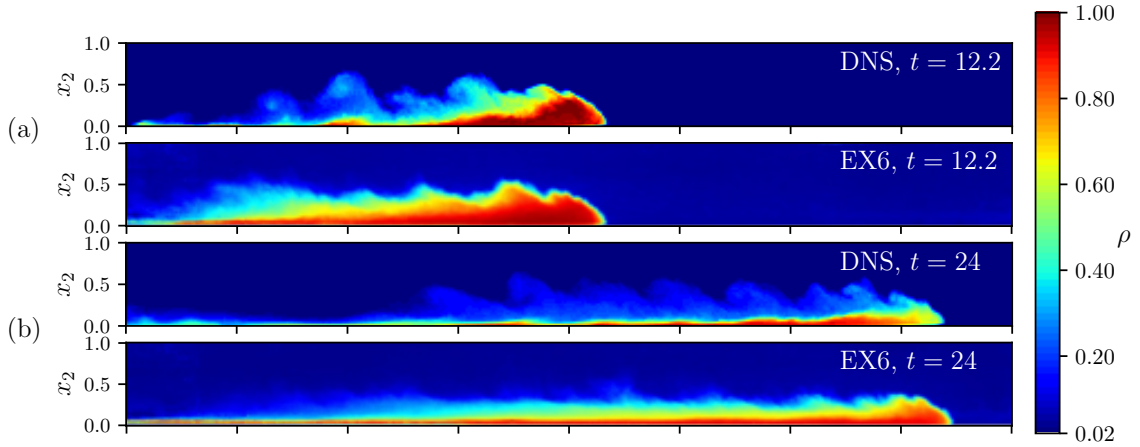


Figure (6) Spanwise-averaged density field for the DNS (top) and EX6 (bottom) for (a) $t = 12.2$ and (b) $t = 24$.

552 consume more energy than in the experiments.

To track the evolution of the front position $x_f(t)$ in the DNS, a simple reverse search is performed on the quantity $\bar{\rho}$ defined as

$$\bar{\rho}(x_1, t) = \int_0^{L_2} \int_0^{L_3} \rho(x_1, x_2, x_3, t) dx_2 dx_3, \quad (33)$$

555 The streamwise position of the front of the current $x_f(t)$ is defined as the first position where $\bar{\rho}(x_1, t) > 0.01$ (starting from the end of the computational domain in the streamwise direction). The associated front velocity $u_f(t)$ is evaluated by calculating the derivative of $x_f(t)$ with respect to time. Figure 7a shows the temporal evolution of $x_f(t)$ for both EX6 and the DNS. The experimental values have been extracted from [Fragoso et al. \(2013\)](#) by using 32 equally-spaced frames from the video provided with the article.
 561 A specific modulation has been used to make sure that the aspect ratio of the video is the same as in the DNS. An excellent agreement between the experiment and the DNS

is obtained for the location of the front position. Note that t_s corresponds to the end of the slumping phase and t_i to the end of the inertial phase.

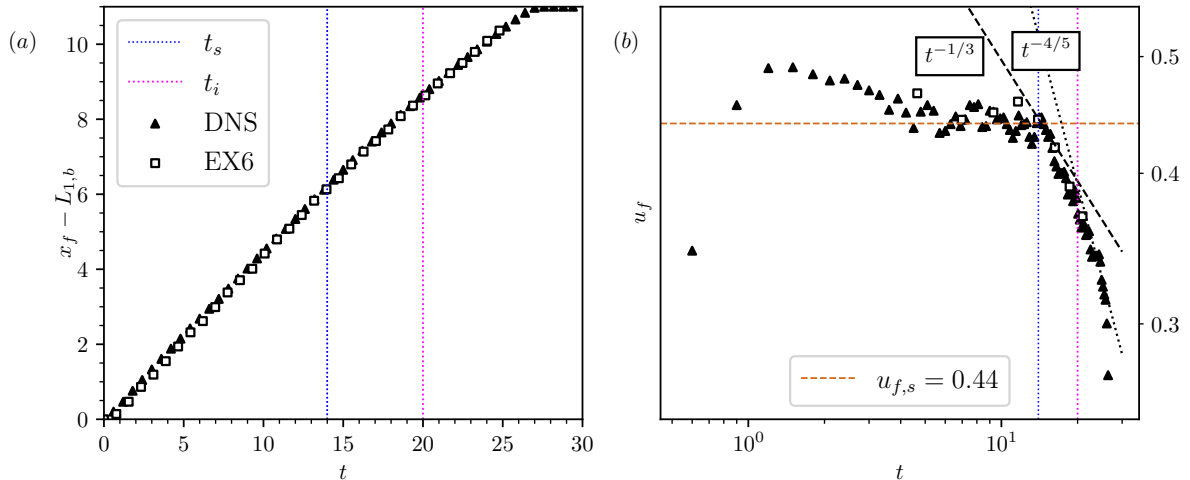


Figure (7) Temporal evolution of the front position (a) and front velocity (b) for the DNS and EX6. t_s corresponds to the end of the slumping phase and t_i to the end of the inertial phase.

The temporal evolution of the front velocity is presented in Figure 7b. For the DNS, the acceleration phase (in which the current initially at rest reaches its maximum velocity) peaks at $t \approx 1.5$ and is followed by a small deceleration phase up to $t \approx 4$. Note that the acceleration phase for the experiment cannot be captured properly due to the coarse temporal resolution from the video and the large perturbations generated by the manual removal of the gate. After $t \approx 4$ and up to $t_s = 14$, both sets of data indicate that the front velocity is nearly constant, corresponding to the slumping phase, with $u_{f,s} = 0.44$. The front velocity then starts to decrease first at a slow rate (inertial phase, up to $t = 21$), then at a fast rate (viscous phase). The current then hit the end of the computational domain for the DNS and the wall at the end of the water tank for the experiment for $t_w \approx 27$. Overall, numerical and experimental data for the front velocity are in good agreement with each other. Several theoretical and empirical models have been proposed to predict the front velocity during the inertial and viscous phases, where the current decelerate following power-law decays, with $u_f \propto t^{-\alpha}$, see Huppert and Simpson (1980); Cantero et al. (2007b). For the inertia phase, it was suggested that $\alpha = 1/3$ and for the viscous phase that $\alpha = 4/5$, values recovered here for both numerical and experimental data as seen in figure 7b.

The dilution of the heavy fluid into the light ambient fluid was carefully investigated in Fragoso et al. (2013) by counting over time areas of the current greater than arbitrary thresholds (using density colour maps for the spanwise-averaged density field). In our DNS, in a similar fashion to Necker et al. (2005), a subarea A^{ρ_1} , where ρ exceeds a certain threshold ρ_1 , can be defined for the spanwise-averaged density field

$$A^{\rho_1}(t) = \int_A (\langle \rho(x_1, x_2, t) \rangle_{x_3} \geq \rho_1) dA. \quad (34)$$

Figure 8a shows the temporal evolution of $A^{\rho_1}/A_0^{\rho_1}$ (where $A_0^{\rho_1} = A^{\rho_1}(t = 0)$) for thresholds $\rho_1 = 0.02, 0.5, 0.8, 0.92$. The initial density field is zero everywhere, except in the

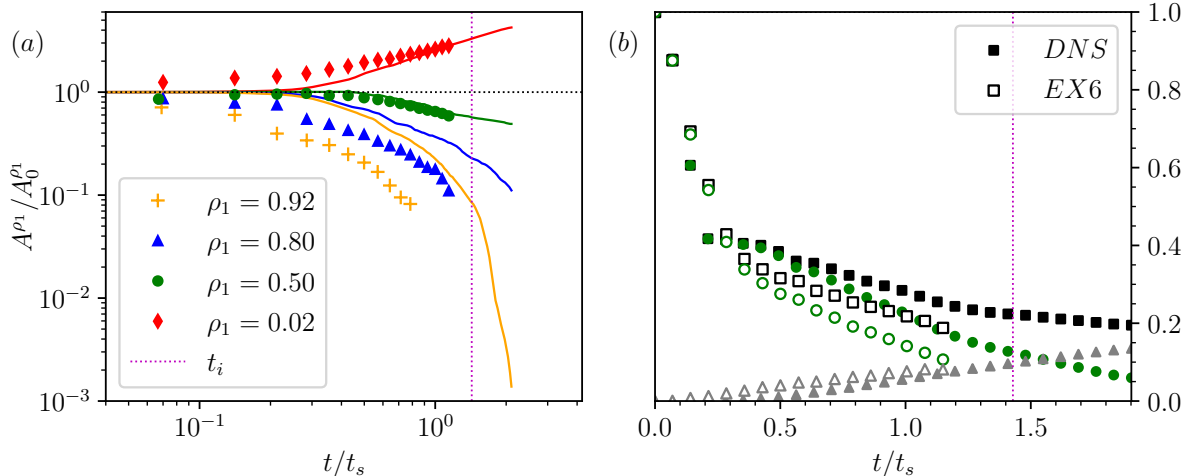


Figure (8) (a) Temporal evolution of $A^{\rho_1}(t)/A_{t=0}^{\rho_1}$ for different density thresholds. The solid lines correspond to the DNS, and the symbols to EX6. (b) Temporal evolution of the normalised energy. Here, the black square symbols correspond to the total potential energy $\mathcal{P}(t)$, the grey triangle symbols to the background potential energy \mathcal{P}_b and the green circle symbols to the difference between the two. Data are normalised so that the minimum total potential energy is zero and the maximum total potential energy is 1. Time is scaled by t_s .

reservoir for which it is equal to 1. In an idealised mixing scenario where the reservoir and the ambient have the same volume, the density field would eventually be equal to 0.5 everywhere (corresponding to a perfect mixing). It is therefore natural to expect $A^{\rho_1}(t)/A_0^{\rho_1}$ to go above/below 1 for thresholds below/above 0.5. In practice, and due to the lock-exchange set-up in the present work, this might not be exactly the case. It also should be noted that the error margin is quite large in the experiments due to the difficulties associated with capturing certain density levels with advanced optical techniques, as mentioned in [Fragoso et al. \(2013\)](#). Furthermore, the manual removal of the gate in the experiments is producing more perturbations than its numerical counterpart based on a numerical white noise (the reader can have a look at the video of the experiments provided with the article). It is therefore anticipated that more stirring and mixing would occur in the experiments soon after removing the gate. As a result, a small time delay (intrinsic to the threshold) is expected: large thresholds for $A^{\rho_1}/A_0^{\rho_1}$ will decay earlier and small thresholds for $A^{\rho_1}/A_0^{\rho_1}$ will increase earlier, by comparison to the simulations. Thresholds around 0.5 should not be affected.

A convincing agreement between the experimental and numerical data can be observed for the threshold 0.5. As expected, the large experimental thresholds for $A^{\rho_1}/A_0^{\rho_1}$ are decaying earlier than the ones in the simulation, however the rate of decay for both the experiment and the simulation are the same for $\rho_1 = 0.8$ and $\rho_1 = 0.92$. It confirms that without a noisy removal of the gate in the experiment or with a noisier artificial perturbation in the simulation, the blue and yellow lines would be on top of the blue and yellow symbols. For the lowest threshold, the agreement between the experiment and the simulation is not so good which confirm that capturing properly very low thresholds in the experiment is challenging due to margin of error of the camera, as mentioned by [Fragoso et al. \(2013\)](#). The present results also confirm that accurate measurements of mixing cannot rely on density threshold methods alone and must include an integral

615 method, such as rearranged potential energy, to characterise the evolution of a continuous
density field, in agreement with the findings of [Fragoso et al. \(2013\)](#).

618 Figure 8b compares the time evolution of total, available and background energy for
EX6 and the DNS. For this figure, each term is normalised so that the minimum total
potential energy is zero and the maximum total potential energy is 1, while the time is
scaled by the time required to reach the slumping distance. The DNS is able to capture
621 the initial strong decay of available energy, up to $t/t_s \approx 0.3$, followed by a more moderate
decay afterwards where the DNS over-predicts the available energy by comparison to the
experiment, with a 15% to 25% difference. It suggests that the noisy removal of the
624 gate in the experiment might have consumed a fair amount of available energy, hence the
lowest values reported in the experiment after $t/t_s \approx 0.5$. Further investigations would be
needed to confirm this point. More details about the behaviour of \mathcal{P}_a and \mathcal{P}_b is provided
627 in the next section.

Overall, the DNS is able to capture accurately the main features of the gravity current,
with a good agreement with the experiment EX6 of [Fragoso et al. \(2013\)](#), except for the
630 temporal evolution of low and high density thresholds. In the following, the DNS will be
used as a reference to evaluate the performance of the LES models.

4. LES results

633 The present study aims to assess the ability of LES to reproduce the main features
of a high-Reynolds number gravity current in a channelised lock-exchange set-up, at a
fraction of the cost of the DNS. In this section, several LES are performed, with the
636 standard Smagorinsky model (SSM), with the dynamic Smagorinsky model (DSM) and
with the SVV model based on high-order finite-difference schemes. The spatial resolution
of the LES has been chosen to be as small as possible while making sure that the LES
639 are stable without any numerical artefact (no limiters to constrain the density field to
values between 0 and 1 or filtering procedures to remove numerical oscillations are used
in the present LES). The spatial resolution for the LES is $n_1 \times n_2 \times n_3 = 577 \times 201 \times 24$
642 mesh nodes, a reduction of more than a factor 7, 3.8 and 10 in the streamwise, vertical
and spanwise directions, respectively, by comparison to the DNS data. Expressed in wall
viscous units, it corresponds to a maximal resolution of $\Delta_{x_{1max}}^+ \approx 10/15$, $\Delta_{x_{2max}}^+ \approx 2$
645 and $\Delta_{x_{3max}}^+ \approx 10/15$. Those values have been obtained by calculating the maximum
value of the spanwise-averaged wall shear velocity at each time step. They are in line
with the recommendations of [Pelmaud et al. \(2018\)](#) who suggested that the first off-wall
648 mesh node should lie in the viscous sublayer of the current at the bottom wall. The
streamwise and spanwise values are much smaller than the values reported in [Ottolenghi
et al. \(2016a\)](#) ($\Delta_{x_{1max}}^+ \approx 50$, $\Delta_{x_{2max}}^+ \approx 1$ and $\Delta_{x_{3max}}^+ \approx 20$). For consistency, the same
651 small time step is used for the DNS and the LES so that temporal discretisation errors
are negligible. It means that the present LES are about 275 times cheaper than the DNS.
The first important result is that the SSM LES and DSM LES are 1.8 and 2.5 times more
654 expensive than the SVV model, respectively, as the latter does not require any explicit
terms in the Navier-Stokes equations nor filtering.

As described in 2.4, the SVV model relies on a physical scaling of the numerical
657 dissipation introduced when evaluating the viscous term of the Navier-Stokes equations.
To estimate the physical scaling of ν_0/ν , the strategy proposed by [Dairay et al. \(2017\)](#) has

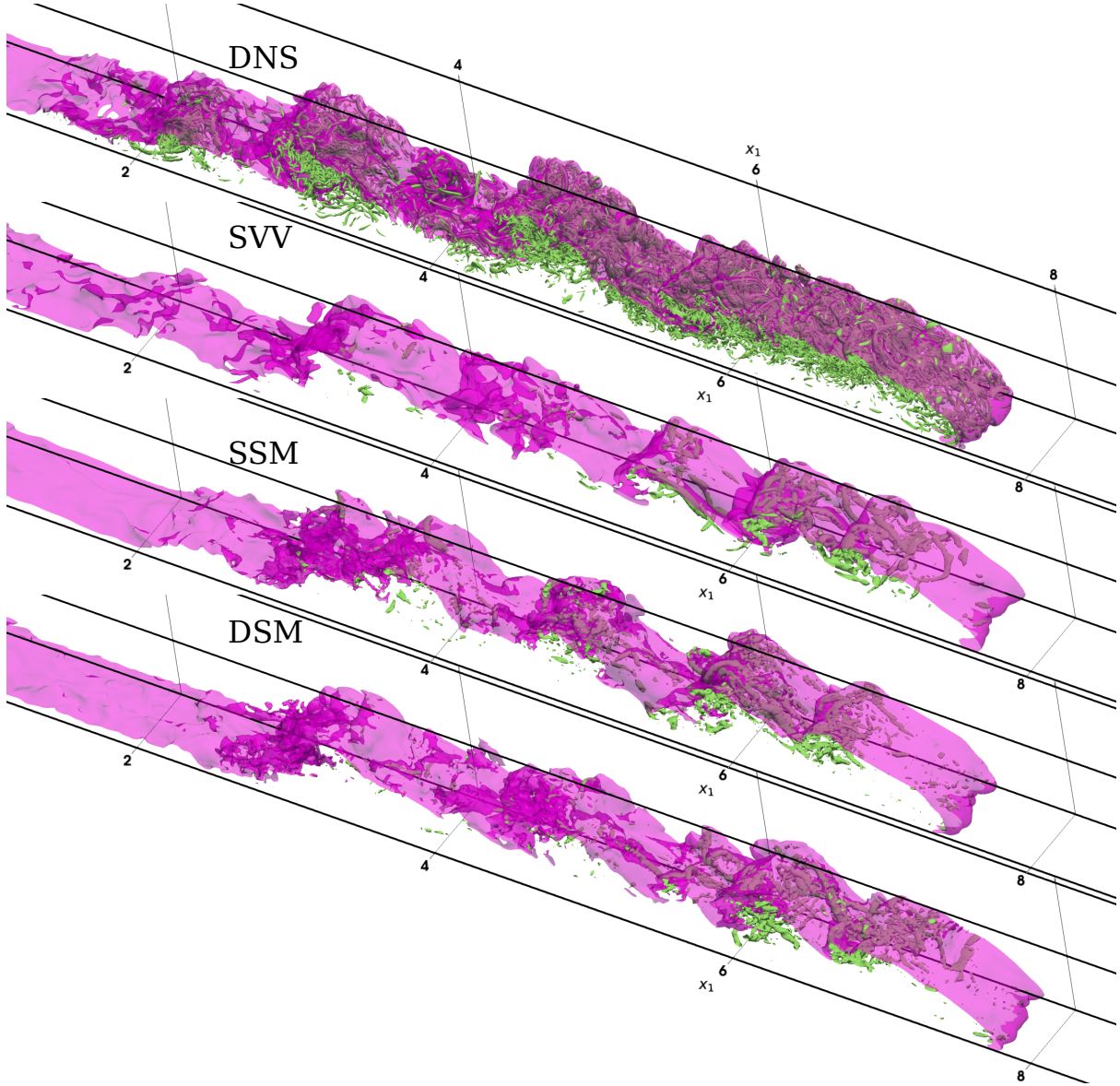


Figure (9) Isocontours of the Q -criterion ($Q = 50$ in green) and the density field $\rho = 0.1$ (pink) at $t = 15$. From top to bottom: DNS, SVV60, SSM and DSM.

660 been used. It is based on a Pao-like spectral closure established on physical arguments to
 661 scale the numerical viscosity. With the current mesh resolution, the theoretical prediction
 of the scaling is $\nu_0/\nu = 60$ (simulation SVV60). It should be noted that this estimate
 662 was designed for homogeneous isotropic turbulence; hence the theoretical prediction of
 this scaling might not be accurate for gravity currents (stratified transitional flows in the
 663 presence of a wall). A sensitivity analysis is presented in [Appendix A](#). It can be seen
 that for the range of ν_0/ν investigated, the quality of the results does not change much
 664 when compared to the DNS data of reference.

4.1. Instantaneous data

665 In figure 9 iso-contours of Q -criterion = 50 and of $\rho = 0.01$ are presented for $t = 15$,
 when the current has reached a fully turbulent state. As expected, a wider range of
 666 turbulent scales can be observed for the DNS, with very fine vortices at the head of the

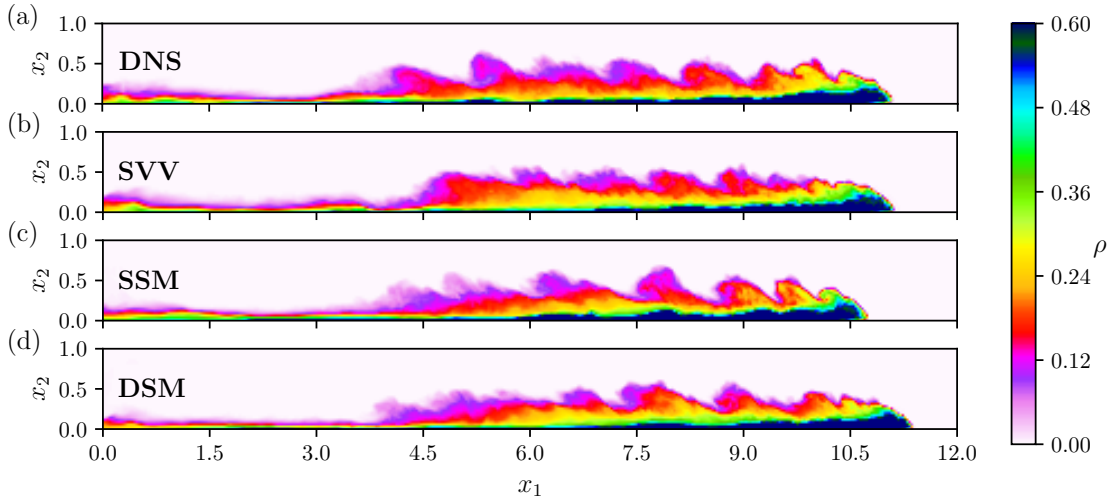


Figure (10) 2D visualisations of the spanwise averaged density field at $t = 24$: (a) DNS, (b) SVV60, (c) SSM, (d) DSM

current and at the interface between the heavy fluid and the lighter fluid. The LES do not produce obvious spurious oscillations, except close to the heavy/light fluid interface for the explicit models (SSM and DSM) for $x_1 \approx 3, 4.5$ and $x_1 \approx 6.5$. At these locations, the streamwise-orientated elongated structures are not as well defined as for the SVV model due to the presence of small non-physical oscillations. The head of the current for the DSM is further ahead than the one in the DNS. For the two explicit LES, the tail of the current (where vortical structures are no longer observable) seems to be further downstream from the inlet than in the SVV LES and DNS.

The spanwise-averaged density field at $t = 24$ is presented in figure 10. It can be seen that the current for the DSM is indeed travelling faster than the current in the DNS while the current in the SSM is travelling slower than the current in the DNS. The LES seems to be able to reproduce properly the main features of the current, in particular the characteristic Kelvin-Helmholtz vortices generated at the head of the current and convected upstream at the heavy/light fluid interface. Furthermore, there seems to be a good agreement between the LES and DNS regarding the different colour thresholds representing different density values.

The friction velocity and associated wall shear stress can be used in a simulation to estimate the critical shear stress level beyond which incipient motion can occur. Such an approach, first introduced by Shields (1936), is based on a similarity method for sediment process, yielding to the Shields diagram. It remains the most widely used strategy to estimate the potential for incipient motion of particles and has been applied in several experimental and numerical works Yalin and Karahan (1979); Ooi et al. (2009); Julien (2010); Tokyay et al. (2012); Tokyay and Constantinescu (2015); Nasr-Azadani and Meiburg (2014); la Forgia et al. (2020). It should be noted however that incipient motion is very often neglected as the configurations studied in laboratory experiments and via high-fidelity simulations cannot replicate the erosion process observed in real-life currents due to the limitation in the Reynolds number. The correct reproduction of the friction velocity is nevertheless an interesting (and challenging to reproduce) quantity of interest to assess the quality of LES models. 2D maps of the friction velocity u^* are presented in

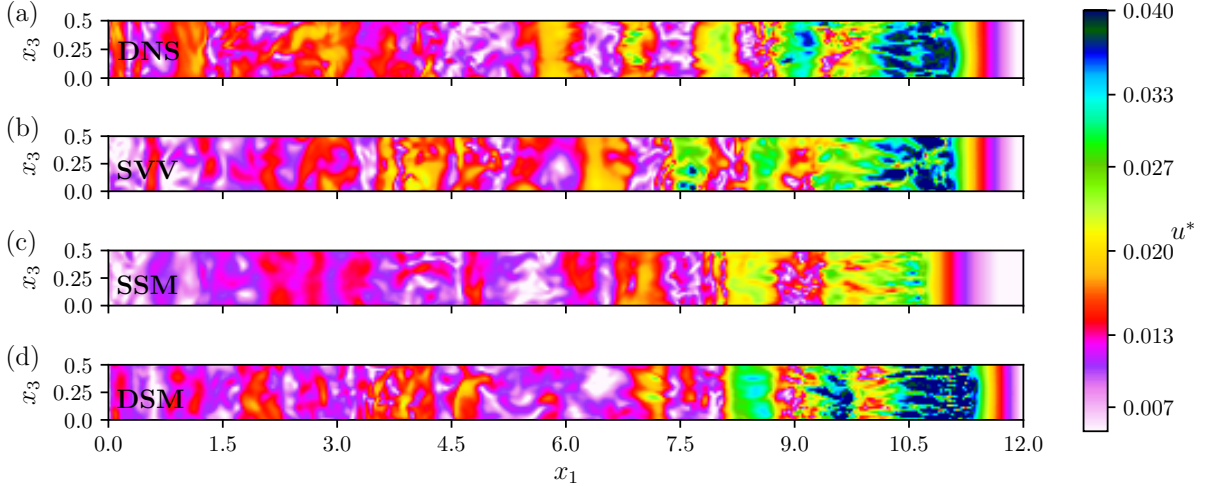


Figure (11) 2D friction velocity maps at $t = 24$: (a) DNS, (b) SVV60, (c) SSM, (d) DSM

figure 11 for $t = 24$. The friction velocity is defined as

$$u^* = \sqrt{\tau_w} \quad \text{with} \quad \tau_w = \frac{1}{Re} \sqrt{\left(\frac{\partial u_1}{\partial x_2}\right)^2 + \left(\frac{\partial u_3}{\partial x_2}\right)^2} \Big|_{x_2=0}. \quad (35)$$

According to figure 11, the best agreement for the friction velocity is obtained for the SVV model, followed by the DSM. The SSM is not able to capture the high values of the friction velocity at the head of the current. It can be connected to a high-level of numerical dissipation at the bottom of the channel. Non-uniformities are observed at the head of the current, a signature of the well-known lobe-and-cleft structures, characterised with intense friction velocities with a streaky pattern (dark blue in the figure). These imprints cannot be captured properly by the SSM.

The formation, merging and meandering of the lobe-and-cleft structures at the front of the current can be seen in figure 12 with iso-lines of the bottom wall density field ($\rho = 0.01$). These structures arise from an instability produced by the ambient fluid, which is overrun by the heavy fluid, and it is one of the main features of gravity currents. As expected, the DNS generates a wider range of lobe-and-cleft structures, with more merging and meandering by comparison to the LES. It seems that less splitting and merging events are present for the explicit LES models as for the SVV model. It is consistent with the overly dissipative behaviour reported in figure 11 for the friction velocity.

4.2. Averaged data

The temporal evolution of the front position and front velocity for the LES is presented in figure 13. As already hinted with the instantaneous visualisation of the current in the previous sub-section, it can be seen that the SSM and DSM are not able to accurately capture the correct location of the front position after the slumping phase. The SVV model is able to capture perfectly the location of the front. The SSM is underestimating the front location, with a deviation from the DNS data starting at the end of the slumping phase. The DSM is slightly overestimating the front location after the slumping phase, in line with the results of Ottolenghi et al. (2016b). Note that an excellent agreement

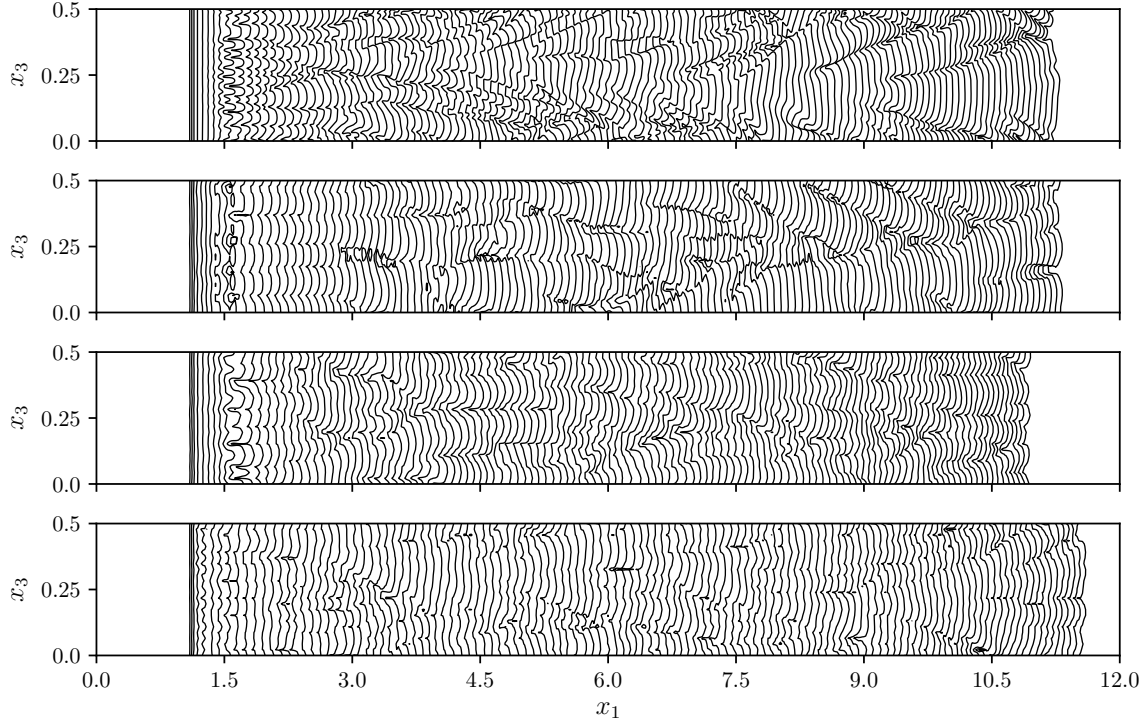


Figure (12) Temporal evolution of the isolines of the bottom wall density field ($\rho = 0.01$) for (a) DNS, (b) SVV60, (c) SSM, (d) DSM.

726 between LES and experiments for the front location was reported in [Ottolenghi et al. \(2018\)](#) but only for very low Reynolds numbers. Despite this minor discrepancy for the SSM, explicit LES models are more or less able to capture the power-law decays when
 729 the current is slowing down, after the slumping phase (the front velocity for the DSM is just slightly higher than the DNS one and it is lower for the SSM).

Figure 14a shows the temporal evolution of the dilution of the heavy fluid into the
 732 ambient fluid by using the same thresholds used in the experiment of [Fragoso et al. \(2013\)](#), see figure 8. It can be seen that all the LES are able to match the DNS data of reference, especially for high thresholds. For the lowest threshold of 0.02, it seems that the DSM
 735 is in slightly better agreement with the DNS, while the dilution for the SVV model and SSM is marginally faster for $\rho_1 = 0.02$.

Figure 14b shows the temporal evolution of the total mass expressed as

$$m_s(t) = \int_V \rho(x_1, x_2, x_3, t) dV. \quad (36)$$

738 It can be seen that all the LES models are capable of conserving the total mass with high accuracy, within less than 0.05%. It suggests that the LES models do not introduce large spurious oscillations to the current. For the explicit LES models, a small amount
 741 of mass is numerically created soon after the release of the heavy fluid, up to $t = 10$ for the DSM and up to $t = 20$ for the SSM. For the DSM, mass is removed from the current from $t = 10$ onward while the mass is more or less conserved for the SSM and the SVV
 744 model. It suggests that the DSM might have an under-dissipative behaviour at the start of the simulation (with a fast-moving current) and an over-dissipative behaviour when the current is fully established.

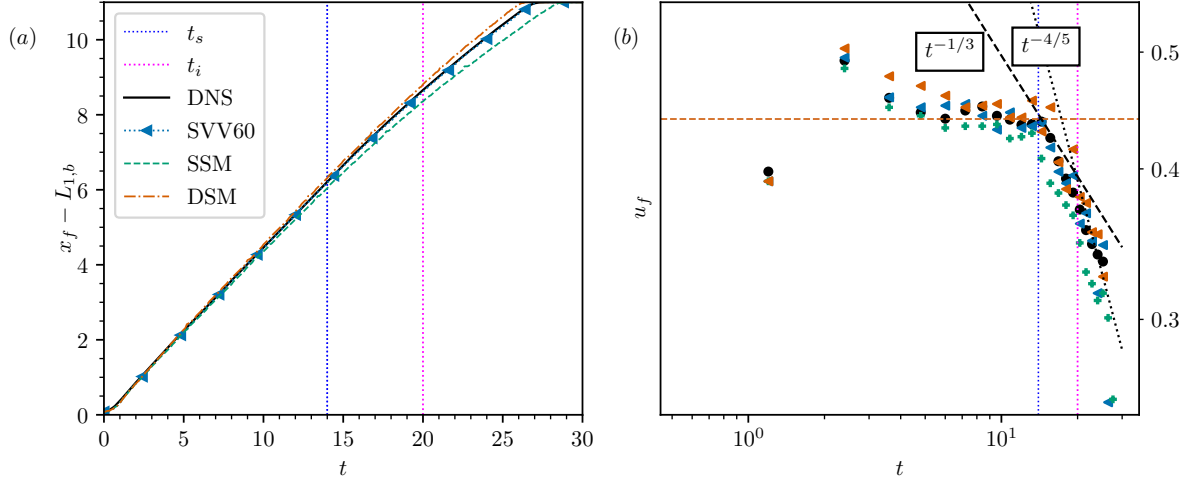


Figure (13) Temporal evolution of the front position (a) and front velocity (b) for the various LES.

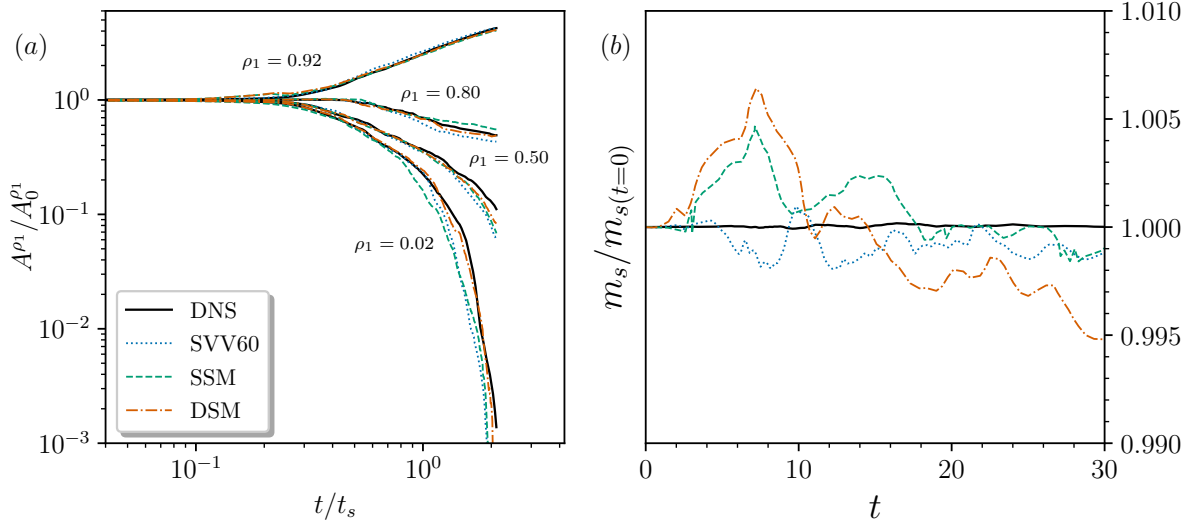


Figure (14) Temporal evolution of the dilution for different thresholds for the density field (a) and the global mass (b) for the DNS and the LES.

747 The total energy budget is presented in figure 15a while the temporal evolution of the
energy transfer mechanisms (vertical buoyancy flux and mixing) is presented in figure
15b. In order to account for the numerical dissipation, the calculation of the internal
750 energy needs to be modified as follow

$$\mathcal{I}(t) = \int_0^t [\epsilon(t) - \Phi(t)] dt + \mathcal{I}_{LES}. \quad (37)$$

Following a strategy introduced in Sun and Domaradzki (2018), \mathcal{I}_{LES} , which accounts
for contribution of the numerical dissipation to the dissipation rate, can be evaluated as
753 a residual

$$\mathcal{I}_{LES}(t) = \mathcal{T}(t=0) - \mathcal{T}(t). \quad (38)$$

The main assumption of this approach is that the energy is perfectly conservation for the
LES. In the DNS, $\mathcal{I}_{LES}(t)$ is of course equal to zero (which is the case in our DNS).

756 It can be seen in figure 15 that at the very early stage of the simulations, there is a
 swift drop of available potential energy \mathcal{P}_a , up to $t \approx 4$, associated with a rapid increase
 of total kinetic energy \mathcal{K} . This rapid increase is produced by a strong vertical buoyancy
 759 flux ϖ as shown in figure 15b. Over 50% of the available potential energy is transferred
 into total kinetic energy. It corresponds to the important amount of energy used by
 the current to establish itself following the removal of the gate. Very little irreversible
 762 dyapicnal mixing ϱ , defined as an irreversible energy transfer mechanism acting towards
 smoothing the density field, is occurring at the start of the simulations, which is consistent
 with a quasi-steady background energy (only diabatic mixing can produce changes in the
 765 background state, see Winters et al. (1995)).

After the peak of total kinetic energy, the available potential energy and total ki-
 netic energy exhibit a steady decay, associated with an increase in internal energy and
 768 background potential energy associated with a sustained mixing activity (with ϱ nearly
 constant). The vertical buoyancy flux ϖ and viscous dissipation ε are steadily decreasing
 after the total kinetic energy peak, while the density diffusion Φ is increasing and the
 771 irreversible dyapicnal mixing ϱ is more or less steady. The small increase in available
 potential energy and the sudden decrease in total kinetic energy at the end of the simula-
 tions are linked to the current reaching the end of the computational domain for $t \approx 27$.
 774 By the end of the simulation, the available potential energy is as low as 10% of its ini-
 tial value. Most of the available potential energy has been converted as internal energy
 (more than 50%). The main mechanism of transfer of energy is the vertical buoyancy
 777 flux, which is more or less two orders of magnitude larger than the density diffusion, one
 order of magnitude larger than the irreversible dyapicnal mixing, and much larger than
 the viscous dissipation.

780 Overall, all the LES are able to reproduce the energy budget and the evolution of
 the transfer mechanisms obtained in the DNS, with only minor differences such as an
 over-estimation of the internal energy for the SSM model of about 10 – 15%, associated
 783 with a slight under-prediction of the total kinetic energy of about 5 – 10%. It is a
 confirmation that the SSM is possibly too dissipative (\mathcal{I}_{LES} is much larger for the SSM
 than for the DSM), especially in high shear/low turbulence regions. The DSM and SVV
 786 model have a consistent behaviour, with a similar amount of numerical dissipation added
 to the current and only a marginal over-estimation of the internal energy for the DSM
 with respect to the DNS. As expected, the viscous dissipation ε is under-predicted in the
 789 LES by comparison to the DNS as ε is computed with first order derivatives for which
 there is no added numerical dissipation. ε is slightly more under-predicted for the SSM
 than for the DSM and SVV model. The LES seem to be able to capture accurately
 792 the available and background potential energy from the DNS. A similar observation was
 already reported in Oezgoekmen et al. (2009) where the background potential energy
 was used to assess the performance of 6 different LES models for lock-exchange gravity
 795 currents. A small peak of insignificant importance for the dynamic of the current (two
 order of magnitude small than the vertical buoyancy flux ϖ) can be observed in for ϱ
 and Φ at $t \approx 3$. This peak is over-estimated in the LES by comparison to the DNS,
 798 especially for the DSM, however with virtually no impact on the temporal evolution of
 the energy transfer mechanisms after the peak (confirmed by the good agreement with
 the DNS data).

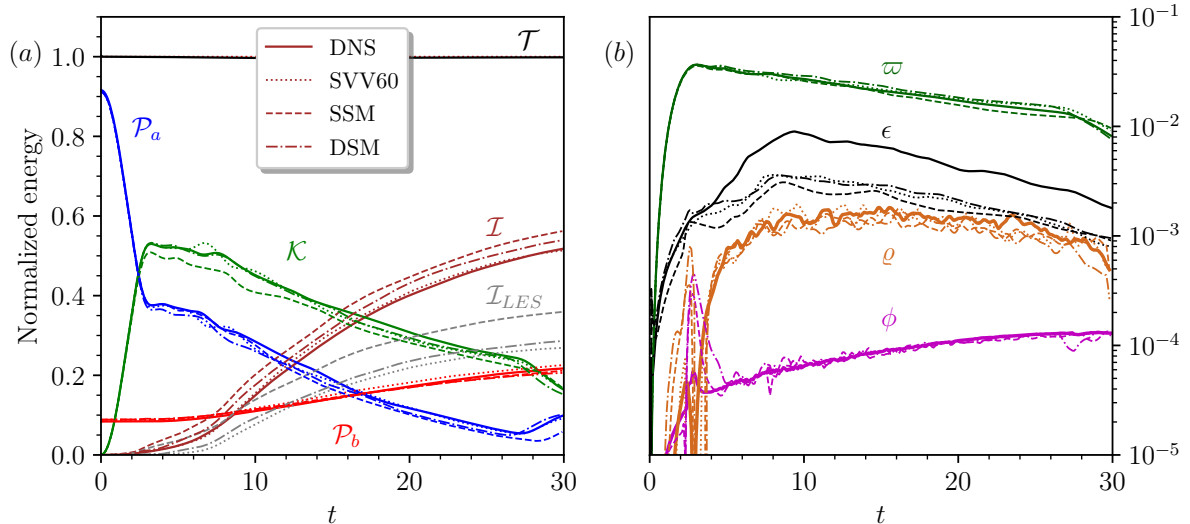


Figure (15) Temporal evolution of the energy budget normalised by the total initial energy (a) and the energy transfer mechanisms (b). The solid lines corresponds to the DNS, the dotted lined to the SVV60, the dashed lines to the SSM and the dash-dotted lines to the DSM.

801 5. Conclusions

In this numerical study, high-fidelity simulations of a gravity current in the lock-exchange set-up have been performed and compared with experimental data. The potential of using a high-order finite-difference SVV approach in the context of LES was investigated with a detailed comparison with more conventional LES based on explicit SGS model and with a resolved DNS. The DNS was performed with more than 800 million mesh nodes and is to the best of our knowledge, one of the DNS of gravity currents in a lock-exchange set-up with the highest Reynolds number. The LES were performed with only less than 0.4% of the total number of mesh nodes of the DNS. An original energy framework was introduced to better understand the main features of the gravity currents.

The main conclusion is that all LES models are good enough to reproduce the main features of the gravity currents, with, however, slightly better performance for the SVV model, in particular close to the bottom of the channel. It should be noted that the SVV model does not require any filtering nor the computation of extra terms in the Navier-Stokes equations, making it very competitive in terms of computational cost (the SSM and DSM are 1.8 and 2.5 times more expensive than the SVV model, respectively). The SVV model is therefore up-and-coming for future high-fidelity simulations of gravity currents at much higher Reynolds numbers, with the potential to reach real-life parameters.

Our next study will focus on high-fidelity simulations of high Reynolds numbers Boussinesq gravity currents, thanks to the flow solver `QuasIncompact3D`, part of the `Xcompact3d` framework. This solver is based on the compressible Navier-Stokes equations in the low Mach number limit, allowing simulations of gravity currents with densities ratio of up to 10 between the heavy release and the ambient fluid (Bartholomew and Laizet, 2019). High Reynolds numbers non-Boussinesq gravity currents in a basin set-up (where the current can freely evolve in the spanwise and streamwise directions, see Francisco et al. (2018)) will also be investigated.

828 It could also be of interest to investigate the potential of the present SVV model for
turbulent flows where the mixing aspect is dominant, such as turbulent flows induced
by Rayleigh-Taylor instabilities (Zhou, 2017a,b; Zhou et al., 2019). A two-phase flow
831 solver based on the Allen-Cahn phase-field approach is currently under development
within the `Xcompact3D` framework, as an extension of the existing `QuasIncompact3D` flow
solver. This will allow us to study turbulent mixing induced by hydrodynamic instabilities
834 such as the Rayleigh-Taylor, Richtmyer-Meshkov, and Kelvin-Helmholtz instabilities with
potential applications in astrophysics, geophysics, and other engineering flows of both
scientific interest and practical significance.

837 Appendix A. Sensitivity study for the SVV model

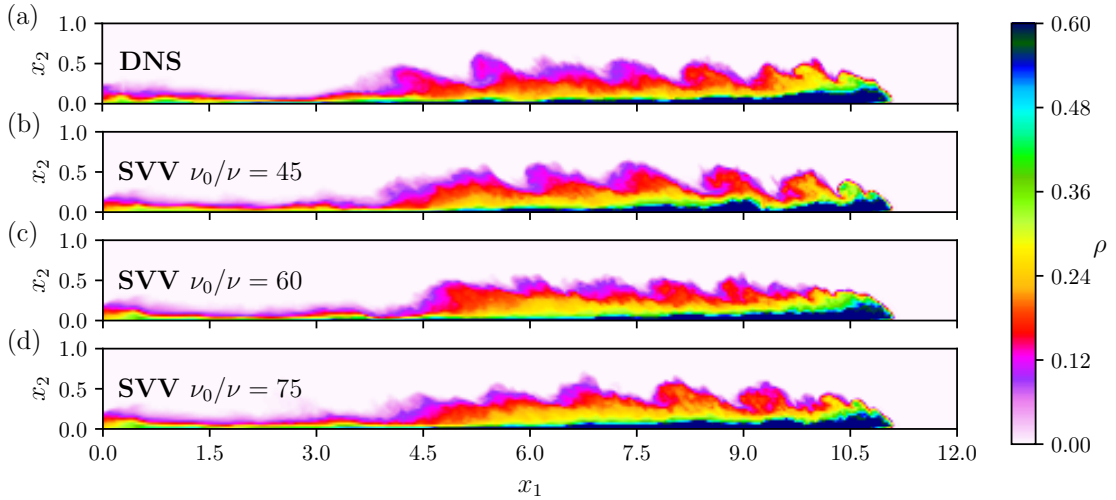


Figure (A.16) 2D visualisations of the spanwise averaged density field at $t = 24$ for the DNS and SVV45, SVV60 and SVV75.

To investigate the sensitivity of ν_0/ν for the present lock-exchange set-up, five extra
LES have been performed with ν_0/ν ranging from 15 to 90, with increment of 15 (sim-
840 ulations SVV15 to SVV90). Figure A.16 shows spanwise-averaged visualisations of the
density field at $t = 24$ for SVV45, SVV60 and SVV75. Overall, an excellent agreement
with the DNS data of reference can be seen with very little difference when the numerical
843 dissipation is changed. No spurious oscillations can be observed suggesting that enough
numerical dissipation is added at small scales, even for SVV45. It should be noted that
no numerical artefact is applied to the density field (no filtering nor limiters).

846 The front location and front velocity for the various SVV simulations are in excellent
agreement with the DNS data of reference, as seen in figure A.17. Actually, all the SVV
simulations are in better agreement with the DNS data than the explicit LES models.
849 It is another evidence that the SVV model is not sensitive to ν_0/ν , as long as enough
numerical dissipation is added to the flow.

Figure A.18a compares the temporal evolution of the dilution of the current for four
852 thresholds, in a similar fashion to figure 14a. Once again, it can be seen that changing
 ν_0/ν does not affect the dilution of the heavy fluid in the ambient fluid. All the SVV
models are in excellent agreement with the DNS data of reference, except maybe for the

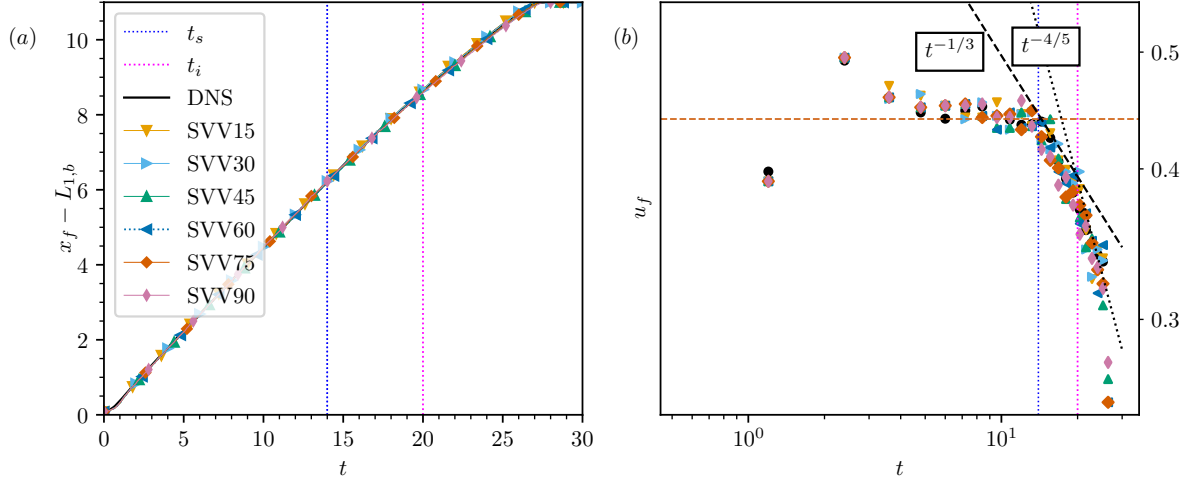


Figure (A.17) Temporal evolution of the front position (a) and front velocity (b) for the DNS and the various LES based on the SVV approach.

855 lowest threshold $\rho_1 = 0.02$ for which all the SVV models are marginally under-predicting
the DNS data, with a slightly faster decay rate. The same observation can be drawn for
the global mass which is perfectly conserved within 0.5%. It is, however clear that SVV15
858 is the simulation with the less accurate results. For the range of numerical dissipation
considered here, the gravity current shows low sensitivity to the choice of ν_0/ν . The small
discrepancies in figure A.18 can be attributed to discretisation errors.

861 Overall, the method proposed by [Dairay et al. \(2017\)](#) to estimate the physical scaling
of ν_0/ν seems to be perfectly capable of providing an adequate value numerical dissipation
for the SVV model, even if it is designed for homogeneous isotropic turbulence. Another
864 important observation is that adding too much numerical dissipation does not seem to
affect the quality of the solution. It will however affect the stability of the simulation.
The use of high values for ν_0/ν would require very small time steps because of the stability
867 limit $\nu\Delta t/\Delta x^2 < \sigma_r/(\nu_0/\nu)\pi^2$ (with for instance $\sigma_r = 2.5$ for a third-order Runge-Kutta
scheme, see [Lamballais et al. \(2011\)](#)).

Acknowledgements

870 The authors acknowledge the National Laboratory for Scientific Computing (LNC-
C/MCTI, Brazil) for providing HPC resources of the [SDumont supercomputer](#) and EP-
SRC for access to the UK Supercomputing facility [ARCHER](#) via the UK Turbulence
873 Consortium (EP/R029326/1). This study was funded by Petrobras and in part by the
Coordenação de Aperfeiçoamento de Pessoal de Nível Superior – Brasil (CAPES) – Fi-
nance Code 001. The authors gratefully acknowledge Bruno A. Farenzena for his helpful
876 insights for the energy budget analysis.

References

- Allen, J., 2012. Principles of physical sedimentology. Springer Science & Business Media.
- 879 Armenio, V., Sarkar, S., 2002. An investigation of stably stratified turbulent channel flow
using large-eddy simulation. *Journal of fluid mechanics* 459, 1–42.

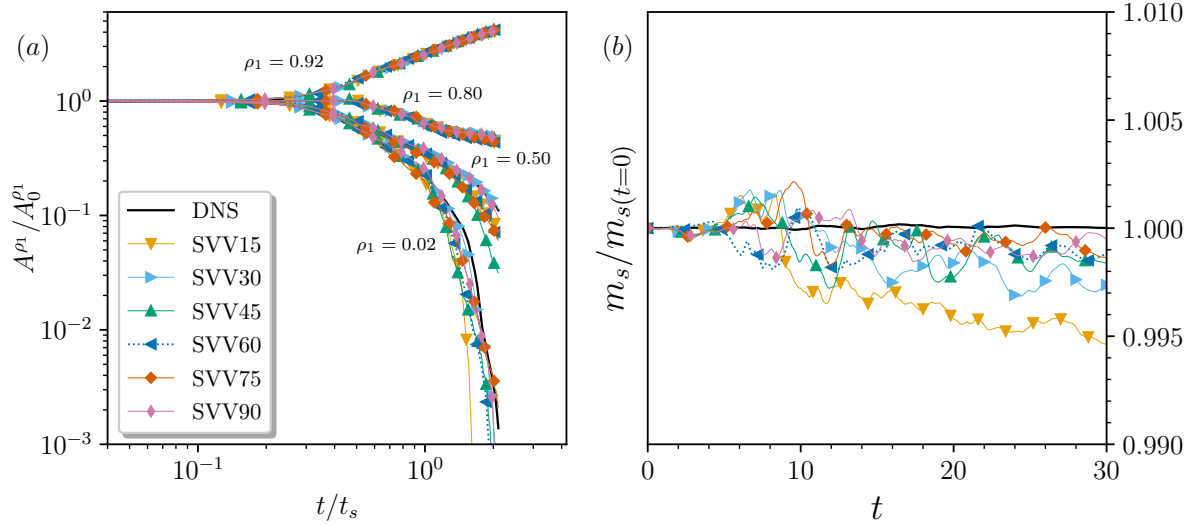


Figure (A.18) Temporal evolution of the dilution for different thresholds for the density field (a) and of the global mass (b) for the DNS and the various LES based on the SVV approach.

Bartholomew, P., Deskos, G., Frantz, R.A., Schuch, F.N., Lamballais, E., Laizet, S.,
 882 2020. Xcompact3d: An open-source framework for solving turbulence problems on a
 cartesian mesh. *SoftwareX* 12, 100550.

Bartholomew, P., Laizet, S., 2019. A new highly scalable, high-order accurate framework
 885 for variable-density flows: Application to non-boussinesq gravity currents. *Computer
 Physics Communications* 242, 83 – 94.

Bonnetaze, R., Huppert, H., Lister, J., 1993. Particle-driven gravity currents. *J. Fluid
 888 Mech.* 250, 339–369.

Bonometti, T., Balachandar, S., 2008. Effect of schmidt number on the structure and
 propagation of density currents. *Theoretical and Computational Fluid Dynamics* 22,
 891 341.

Boris, J., Grinstein, F., Oran, E., Kolbe, R., 1992. New insights into large eddy simula-
 tion. *Fluid dynamics research* 10, 199–228.

894 Britter, R., Linden, P., 1980. The motion of the front of a gravity current travelling down
 an incline. *Journal of Fluid Mechanics* 99, 531–543.

Britter, R., Simpson, J., 1978. Experiments on the dynamics of a gravity current head.
 897 *J. Fluid Mech.* 88, 223–240.

Cantero, M., Balachandar, S., Garcia, M., 2007a. High-resolution simulations of cylin-
 drical density currents. *Journal of Fluid Mechanics* 590, 437–469.

900 Cantero, M., Lee, J., Balachandar, S., Garcia, M., 2007b. On the front velocity of gravity
 currents. *J. Fluid Mech.* 586, 1–39.

- 903 Cantero, M.I., Balachandar, S., García, M.H., Bock, D., 2008. Turbulent structures in planar gravity currents and their influence on the flow dynamics. *Journal of Geophysical Research: Oceans* 113.
- 906 Canuto, C., Hussaini, M.Y., Quarteroni, A., Thomas Jr, A., et al., 2012. *Spectral methods in fluid dynamics*. Springer Science & Business Media.
- Cerutti, S., Meneveau, C., Knio, O.M., 2000. Spectral and hyper eddy viscosity in high-reynolds-number turbulence. *Journal of Fluid Mechanics* 421, 307–338.
- 909 Chawdhary, S., Khosronejad, A., Christodoulou, G., Sotiropoulos, F., 2018. Large eddy simulation of density current on sloping beds. *International Journal of Heat and Mass Transfer* 120, 1374–1385.
- 912 Chollet, J.P., Lesieur, M., 1981. Parameterization of small scales of three-dimensional isotropic turbulence utilizing spectral closures. *Journal of the Atmospheric Sciences* 38, 2747–2757.
- 915 Chow, F.K., Moin, P., 2003. A further study of numerical errors in large-eddy simulations. *Journal of Computational Physics* 184, 366 – 380.
- 918 Constantinescu, G., 2014. LES of lock-exchange compositional gravity currents: a brief review of some recent results. *Environmental Fluid Mechanics* 14, 295–317.
- Dairay, T., Fortuné, V., Lamballais, E., Brizzi, L., 2014. LES of a turbulent jet impinging on a heated wall using high-order numerical schemes. *International Journal of Heat and Fluid Flow* 50, 177–187.
- 921 Dairay, T., Lamballais, E., Laizet, S., Vassilicos, J.C., 2017. Numerical dissipation vs. subgrid-scale modelling for large eddy simulation. *Journal of Computational Physics* 337, 252–274.
- 924 De Falco, M., Adduce, C., Negretti, M., Hopfinger, E., 2021. On the dynamics of quasi-steady gravity currents flowing up a slope. *Advances in Water Resources* 147, 103791.
- 927 De Falco, M., Ottolenghi, L., Adduce, C., 2020. Dynamics of gravity currents flowing up a slope and implications for entrainment. *Journal of Hydraulic Engineering* 146, 04020011.
- 930 de Rooij, F., Dalziel, S., 2001. Time- and space-resolved measurements of deposition under turbidity currents. *Spec. Pubs. Int. Ass. Sediment.* 31, 207–215.
- 933 Deskos, G., Laizet, S., Palacios, R., 2020. Winc3d: A novel framework for turbulence-resolving simulations of wind farm wake interactions. *Wind Energy* 23, 779–794.
- Deskos, G., Laizet, S., Piggott, M.D., 2019. Turbulence-resolving simulations of wind turbine wakes. *Renewable Energy* 134, 989 – 1002.
- 936 Ellison, T.H., Turner, J.S., 1959. Turbulent entrainment in stratified flows. *Journal of Fluid Mechanics* 6, 423–448.

- Emami, S.M.K., Mousavi, S.F., Hosseini, K., Fouladfar, H., Mohammadian, M., 2020.
939 Comparison of different turbulence models in predicting cohesive fluid mud gravity
current propagation. *International Journal of Sediment Research* .
- Espath, L.F.R., Pinto, L.C., Laizet, S., Silvestrini, J.H., 2014. Two- and three-
942 dimensional direct numerical simulation of particle-laden gravity currents. *Computers
& Geosciences* 63, 9 – 16.
- Espath, L.F.R., Pinto, L.C., Laizet, S., Silvestrini, J.H., 2015. High-fidelity simulations of
945 the lobe-and-cleft structures and the deposition map in particle-driven gravity currents.
Physics of Fluids 27, 056604.
- Falkovich, G., 1994. Bottleneck phenomenon in developed turbulence. *Physics of Fluids*
948 6, 1411–1414.
- la Forgia, G., Tokyay, T., Adduce, C., Constantinescu, G., 2018. Numerical investigation
of breaking internal solitary waves. *Physical Review Fluids* 3, 104801.
- 951 la Forgia, G., Tokyay, T., Adduce, C., Constantinescu, G., 2020. Bed shear stress and
sediment entrainment potential for breaking of internal solitary waves. *Advances in
Water Resources* 135, 103475.
- 954 Fragoso, A.T., Patterson, M.D., Wettlaufer, J.S., 2013. Mixing in gravity currents. *Jour-
nal of Fluid Mechanics* 734, R2.
- Francisco, E.P., Espath, L.F.R., Laizet, S., Silvestrini, J.H., 2018. Reynolds number and
957 settling velocity influence for finite-release particle-laden gravity currents in a basin.
Computers & Geosciences 110, 1–9.
- Germano, M., Piomelli, U., Moin, P., Cabot, W.H., 1991. A dynamic subgrid-scale eddy
960 viscosity model. *Physics of Fluids A: Fluid Dynamics* 3, 1760–1765.
- Ghosal, S., 1996. An analysis of numerical errors in large-eddy simulations of turbulence.
Journal of Computational Physics 125, 187 – 206.
- 963 Gladstone, C., Phillips, J.C., Sparks, R.S.J., 1998. Experimentation on bidisperse,
constant-volume gravity currents: propagation and sediment deposition. *Sedimentology*
46, 833–843.
- 966 Gonzalez-Juez, E., Meiburg, E., Tokyay, T., Constantinescu, G., 2010. Gravity current
flow past a circular cylinder: forces, wall shear stresses and implications for scour.
Journal of Fluid Mechanics 649, 69–102.
- 969 Grinstein, F.F., Fureby, C., 2004. From canonical to complex flows: Recent progress on
monotonically integrated les. *Computing in Science Engineering* 6, 36–49.
- Grundy, R., Rottmant, J.W., 1986. Self-similar solutions of the shallow-water equations
972 representing gravity currents with variable inflow. *Journal of Fluid Mechanics* 169,
337–351.

- 975 Härtel, C., Kleiser, L., Michaud, M., Stein, C., 1997. A direct numerical simulation approach to the study of intrusion fronts. *Journal of engineering mathematics* 32, 103–120.
- 978 Härtel, C., Meiburg, E., Necker, F., 2000. Analysis and direct numerical simulation of the flow at a gravity-current head. Part 1. Flow topology and front speed for slip and no-slip boundaries. *J. Fluid Mech.* 418, 189–212.
- 981 Haugen, N.E.L., Brandenburg, A., 2004. Inertial range scaling in numerical turbulence with hyperviscosity. *Phys. Rev. E* 70, 026405.
- Huppert, H., Simpson, J., 1980. The slumping of gravity currents. *J. Fluid Mech.* 99(04), 785–799.
- 984 Inghilesi, R., Adduce, C., Lombardi, V., Roman, F., Armenio, V., 2018. Axisymmetric three-dimensional gravity currents generated by lock exchange. *Journal of Fluid Mechanics* 851, 507–544.
- 987 Ioannou, V., Laizet, S., 2018. Numerical investigation of plasma-controlled turbulent jets for mixing enhancement. *International Journal of Heat and Fluid Flow* 70, 193 – 205.
- Julien, P., 2010. *Erosion and sedimentation*. Cambridge University Press.
- 990 Karamanos, G., Karniadakis, G.E., 2000. A spectral vanishing viscosity method for large-eddy simulations. *Journal of Computational Physics* 163, 22–50.
- 993 Kirby, R., Karniadakis, G., 2002. Coarse resolution turbulence simulations with spectral vanishing viscosity – large-eddy simulations (svv-les). *ASME. J. Fluids Eng.* 124.
- Kraichnan, R.H., 1976. Eddy viscosity in two and three dimensions. *Journal of the Atmospheric Sciences* 33, 1521–1536.
- 996 Kravchenko, A., Moin, P., 1997. On the effect of numerical errors in large eddy simulations of turbulent flows. *Journal of computational physics* 131, 310–322.
- 999 Kyrousi, F., Leonardi, A., Roman, F., Armenio, V., Zanello, F., Zordan, J., Juez, C., Falcomer, L., 2018. Large eddy simulations of sediment entrainment induced by a lock-exchange gravity current. *Advances in Water Resources* 114, 102–118.
- 1002 Laizet, S., Lamballais, E., 2009. High-order compact schemes for incompressible flows: A simple and efficient method with the quasi-spectral accuracy. *J. Comp. Phys.* 228, 5989–6015.
- 1005 Laizet, S., Li, N., 2011. Incompact3d: A powerful tool to tackle turbulence problems with up to $O(10^5)$ computational cores. *Int. J. Numer. Methods Fluids* 67, 1735–1757.
- 1008 Lamballais, E., Fortune, V., Laizet, S., 2011. Straightforward high-order numerical dissipation via the viscous term for direct and large eddy simulation. *J. Comp. Phys.* 230(9), 3270–3275.

- Lele, S.K., 1992. Compact finite difference schemes with spectral-like resolution. *J. Comp. Phys.* 103, 16–42.
- 1011 Lesieur, M., Metais, O., 1996. New trends in large-eddy simulations of turbulence. *Annual Review of Fluid Mechanics* 28, 45–82.
- 1014 Lesieur, M., Rogallo, R., 1989. Large-eddy simulation of passive scalar diffusion in isotropic turbulence. *Physics of Fluids A: Fluid Dynamics* 1, 718–722.
- 1017 Lilly, D.K., 1966. The representation of small-scale turbulence in numerical simulation experiments, in: *IBM Scientific Computing Symposium on Environmental Sciences*, Thomas J. Watson Research Center, Yorktown. pp. 195–210.
- Lilly, D.K., 1992. A proposed modification of the germano subgrid-scale closure method. *Physics of Fluids A: Fluid Dynamics* 4, 633–635.
- 1020 Lorenz, E.N., 1955. Available potential energy and the maintenance of the general circulation. *Tellus* 7, 157–167.
- 1023 Lucchese, L.V., Monteiro, L.R., Schettini, E.B.C., Silvestrini, J.H., 2019. Direct numerical simulations of turbidity currents with evolutive deposit method, considering topography updates during the simulation. *Computers & Geosciences* 133, 104306.
- 1026 Mahdinia, M., Firoozabadi, B., Farshchi, M., Varnamkhasti, A.G., Afshin, H., 2011. Large eddy simulation of lock-exchange flow in a curved channel. *Journal of Hydraulic Engineering* 138, 57–70.
- 1029 Martin, A., Negretti, M., Ungarish, M., Zemach, T., 2020. Propagation of a continuously supplied gravity current head down bottom slopes. *Physical Review Fluids* 5, 054801.
- 1032 Martin, A., Negretti, M.E., Hopfinger, E.J., 2019. Development of gravity currents on slopes under different interfacial instability conditions. *Journal of Fluid Mechanics* 880, 180–208.
- Meiburg, E., Radhakrishnan, S., Nasr-Azadani, M., 2015. Modeling gravity and turbidity currents: computational approaches and challenges. *Applied Mechanics Reviews* 67.
- 1035 Meneveau, C., Katz, J., 2000. Scale-invariance and turbulence models for large-eddy simulation. *Annual Review of Fluid Mechanics* 32, 1–32.
- 1038 Meneveau, C., Lund, T.S., 1997. The dynamic smagorinsky model and scale-dependent coefficients in the viscous range of turbulence. *Physics of Fluids* 9, 3932–3934.
- Meneveau, C., Lund, T.S., Cabot, W.H., 1996. A lagrangian dynamic subgrid-scale model of turbulence. *Journal of fluid mechanics* 319, 353–385.
- 1041 Métais, O., Lesieur, M., 1992. Spectral large-eddy simulation of isotropic and stably stratified turbulence. *Journal of Fluid Mechanics* 239, 157–194.
- 1044 Nasr-Azadani, M., Meiburg, E., 2014. Turbidity currents interacting with three-dimensional seafloor topography. *J. Fluid Mech.* 745, 409–443.

- Necker, F., Hartel, C., Kleiser, L., Meiburg, E., 2002. High-resolution simulations of particle-driven gravity currents. *Int. J. of Multiphase Flow* 28, 279–300.
- 1047 Necker, F., Härtel, C., Kleiser, L., Meiburg, E., 2005. Mixing and dissipation in particle-driven gravity currents. *J. Fluid Mech.* 545, 339–372.
- Nogueira, H.I., Adduce, C., Alves, E., Franca, M.J., 2014. Dynamics of the head of
1050 gravity currents. *Environmental Fluid Mechanics* 14, 519–540.
- Oezgoekmen, T.M., Iliescu, T., Fischer, P.F., 2009. Large eddy simulation of stratified mixing in a three-dimensional lock-exchange system. *Ocean Modelling* 26, 134–155.
- 1053 Ooi, S.K., Constantinescu, G., Weber, L., 2009. Numerical simulations of lock-exchange compositional gravity current. *Journal of Fluid Mechanics* 635, 361–388.
- Ottolenghi, L., Adduce, C., Inghilesi, R., Armenio, V., Roman, F., 2016a. Entrainment
1056 and mixing in unsteady gravity currents. *Journal of Hydraulic Research* 54, 541–557.
- Ottolenghi, L., Adduce, C., Inghilesi, R., Roman, F., Armenio, V., 2016b. Mixing in lock-release gravity currents propagating up a slope. *Physics of Fluids* 28, 056604.
- 1059 Ottolenghi, L., Cenedese, C., Adduce, C., 2017. Entrainment in a dense current flowing down a rough sloping bottom in a rotating fluid. *Journal of Physical Oceanography* 47, 485–498.
- 1062 Ottolenghi, L., Prestininzi, P., Montessori, A., Adduce, C., La Rocca, M., 2018. Lattice boltzmann simulations of gravity currents. *European Journal of Mechanics-B/Fluids* 67, 125–136.
- 1065 Özgökmen, T.M., Iliescu, T., Fischer, P.F., 2009. Reynolds number dependence of mixing in a lock-exchange system from direct numerical and large eddy simulations. *Ocean Modelling* 30, 190–206.
- 1068 Pasquetti, R., 2005. Spectral vanishing viscosity method for les: sensitivity to the svv control parameters. *Journal of Turbulence* 6, N12.
- Pasquetti, R., Séverac, E., Serre, E., Bontoux, P., Schäfer, M., 2008. From stratified
1071 wakes to rotor–stator flows by an SVV–LES method. *Theoretical and Computational Fluid Dynamics* 22, 261–273.
- Patterson, M.D., Caulfield, C., McElwaine, J., Dalziel, S., 2006. Time-dependent mixing
1074 in stratified kelvin-helmholtz billows: Experimental observations. *Geophysical research letters* 33.
- Pelmard, J., Norris, S., Friedrich, H., 2018. Les grid resolution requirements for the
1077 modelling of gravity currents. *Computers & Fluids* 174, 256–270.
- Pelmard, J., Norris, S., Friedrich, H., 2020. Statistical characterisation of turbulence for an unsteady gravity current. *Journal of Fluid Mechanics* 901.

- 1080 Pierce, C.D., 2001. Progress-variable approach for large-eddy simulation of turbulent
combustion. Ph.D. thesis. Stanford University.
- Piper, D., Cochonat, P., Morrison, M., 1999. The sequence of events around the epicentre
1083 of the 1929 grand banks earthquake: initiation of the debris flows and turbidity current
inferred from side scan sonar subaqueous sediment density flows: depositional processes
and deposit types. *Sedimentology* 46(1), 79–97.
- 1086 Pope, S., 2000. *Turbulent Flows*. Cambridge University Press.
- van Reeuwijk, M., Krug, D., Holzner, M., 2018. Small-scale entrainment in inclined
gravity currents. *Environmental Fluid Mechanics* 18, 225–239.
- 1089 Roman, F., Stipcich, G., Armenio, V., Inghilesi, R., Corsini, S., 2010. Large eddy sim-
ulation of mixing in coastal areas. *International Journal of Heat and Fluid Flow* 31,
327–341.
- 1092 Rottman, J.W., Simpson, J.E., 1983. Gravity currents produced by instantaneous releases
of a heavy fluid in a rectangular channel. *Journal of Fluid Mechanics* 135, 95–110.
- Sagaut, P., 2006. *Large eddy simulation for incompressible flows: an introduction*.
1095 Springer Science & Business Media.
- Schuch, F.N., Pinto, L.C., Silvestrini, J.H., Laizet, S., 2018. Three-dimensional
turbulence-resolving simulations of the plunge phenomenon in a tilted channel. *Journal*
1098 *of Geophysical Research: Oceans* 123, 4820–4832.
- Sher, D., Woods, A.W., 2015. Gravity currents: entrainment, stratification and self-
similarity. *Journal of Fluid Mechanics* 784, 130–162.
- 1101 Sher, D., Woods, A.W., 2017. Mixing in continuous gravity currents. *Journal of Fluid*
Mechanics 818.
- Shields, A., 1936. *Anwendung der Ahnlichkeitsmechanik und der turbulenz-forschung*
1104 *auf die Geschiebebewegung*. Ph.D. thesis. A Mitteilungen der (Preussischen) Versuch-
sanstalt.
- Shin, J.O., Dalziel, S.B., Linden, P.F., 2004. Gravity currents produced by lock exchange.
1107 *Journal of Fluid Mechanics* 521, 134.
- Simpson, J., 1999. *Gravity Currents: In the Environment and the Laboratory*. In the
Environment and the Lab, Cambridge University Press.
- 1110 Smagorinsky, J., 1963. General circulation experiments with the primitive equations: I.
the basic experiment. *Monthly weather review* 91, 99–164.
- Sun, G., Domaradzki, J.A., 2018. Implicit LES using adaptive filtering. *Journal of*
1113 *Computational Physics* .
- Tadmor, E., 1989. Convergence of spectral methods for nonlinear conservation laws.
SIAM Journal on Numerical Analysis 26, 30–44.

- 1116 Tokyay, T., Constantinescu, G., 2015. The effects of a submerged non-erodible triangular
obstacle on bottom propagating gravity currents. *Physics of fluids* 27, 056601.
- 1119 Tokyay, T., Constantinescu, G., Meiburg, E., 2011. Lock-exchange gravity currents with
a high volume of release propagating over a periodic array of obstacles. *Journal of
Fluid Mechanics* 672, 570–605.
- 1122 Tokyay, T., Constantinescu, G., Meiburg, E., 2012. Tail structure and bed friction velocity
distribution of gravity currents propagating over an array of obstacles. *J. Fluid Mech.*
694, 252–291.
- 1125 Tokyay, T., Constantinescu, G., Meiburg, E., 2014. Lock-exchange gravity currents with
a low volume of release propagating over an array of obstacles. *Journal of Geophysical
Research: Oceans* 119, 2752–2768.
- 1128 Tseng, Y.h., Ferziger, J.H., 2001. Mixing and available potential energy in stratified
flows. *Physics of Fluids* 13, 1281–1293.
- Venayagamoorthy, S., Koseff, J., Ferziger, J., Shih, L., 2003. Testing of RANS turbulence
models for stratified flows based on DNS data. Technical Report. Stanford University.
- 1131 Vreman, A.W., 2004. An eddy-viscosity subgrid-scale model for turbulent shear flow:
Algebraic theory and applications. *Physics of Fluids* 16, 3670–3681.
- 1134 Vreman, B., Geurts, B., Kuerten, H., 1996. Comparison of numerical schemes in large-
eddy simulation of the temporal mixing layer. *International Journal for Numerical
Methods in Fluids* 22, 297–311.
- 1137 Wilson, R.I., Friedrich, H., Stevens, C., 2018. Flow structure of unconfined turbidity
currents interacting with an obstacle. *Environmental Fluid Mechanics* 18, 1571–1594.
- Winters, K.B., Lombard, P.N., Riley, J.J., D’Asaro, E.A., 1995. Available potential
energy and mixing in density-stratified fluids. *Journal of Fluid Mechanics* 289, 115128.
- 1140 Yalin, M., Karahan, E., 1979. Inception of sediment transport. *Journal of the hydraulics
division* 105(11), 1433–1443.
- 1143 Zemach, T., Ungarish, M., Martin, A., Negretti, M.E., 2019. On gravity currents of fixed
volume that encounter a down-slope or up-slope bottom. *Physics of Fluids* 31, 096604.
- Zgheib, N., Bonometti, T., Balanchandar, S., 2015. Direct numerical simulation of cylin-
drical particle-laden gravity currents. *Computers and Fluids* 123, 23–31.
- 1146 Zhou, Y., 2017a. Rayleigh–taylor and richtmyer–meshkov instability induced flow, tur-
bulence, and mixing. i. *Physics Reports* 720, 1–136.
- 1149 Zhou, Y., 2017b. Rayleigh–taylor and richtmyer–meshkov instability induced flow, tur-
bulence, and mixing. ii. *Physics Reports* 723, 1–160.

1152 Zhou, Y., Clark, T.T., Clark, D.S., Gail Glendinning, S., Aaron Skinner, M., Huntington, C.M., Hurricane, O.A., Dimits, A.M., Remington, B.A., 2019. Turbulent mixing and transition criteria of flows induced by hydrodynamic instabilities. *Physics of Plasmas* 26, 080901.